JBC RESEARCH ARTICLE

Toward an understanding of the conformational plasticity of S100A8 and S100A9 Ca^{2+}-binding proteins

Received for publication, February 4, 2022, and in revised form, January 16, 2023 Published, Papers in Press, January 31, 2023, https://doi.org/10.1016/j.jbc.2023.102952

Magdalena Polakowska[1], **Kamil Steczkiewicz**[1], **Roman H. Szczepanowski**[2], and **Aleksandra Wysłouch-Cieszyńska**[1,*]

From the [1]Institute of Biochemistry and Biophysics, Polish Academy of Sciences, Warsaw, Poland; [2]Biophysical and Structural Biology Core Facility, International Institute of Molecular and Cell Biology, Warsaw, Poland

Reviewed by members of the JBC Editorial Board. Edited by Karen Fleming

S100A8 and S100A9 are small, human, Ca^{2+}-binding proteins with multiple intracellular and extracellular functions in signaling, regulation, and defense. The two proteins are not detected as monomers but form various noncovalent homo- or hetero-oligomers related to specific activities in human physiology. Because of their significant roles in numerous medical conditions, there has been intense research on the conformational properties of various S100A8 and S100A9 proteoforms as essential targets of drug discovery. NMR or crystal structures are currently available only for mutated or truncated protein complexes, mainly with bound metal ions, that may well reflect the proteins' properties outside cells but not in other biological contexts in which they perform. Here, we used structural mass spectrometry methods combined with molecular dynamics simulations to compare the conformations of wildtype full-length S100A8 and S100A9 subunits in biologically relevant homo- and heterodimers and in higher oligomers formed in the presence of calcium or zinc ions. We provide, first, rationales for their functional response to changing environmental conditions, by elucidating differences between proteoforms in flexible protein regions that may provide the plasticity of the binding sites for the multiple targets, and second, the key factors contributing to the variable stability of the oligomers. The described methods and a systematic view of the conformational properties of S100A8 and S100A9 complexes provide a basis for further research to characterize and modulate their functions for basic science and therapies.

S100A8 and S100A9 are small (10.8 and 13.1 kDa, respectively) α-helical proteins belonging to the S100 family, which is the largest group of calcium-binding proteins in humans (1). They are involved in various functions connected to cell signaling, regulation, and defense (1, 2). For instance, they are overexpressed and secreted by white blood cells to mediate inflammation by interacting with extracellular receptors, for example, TLR4 and RAGE (3–5). They also form human "nutritional immunity" complexes that deprive bacteria of transition metal ions essential for their growth (6, 7) and are anti-inflammatory in the process of wound healing (8). Inside cells, S100A8 and S100A9 regulate nitric oxide and reactive oxygen species signaling, NADPH oxidase activation, and arachidonic acid transport, and they modulate tubulin and intermediate filament assembly and telomerase activity (2, 4, 9–11). Recent affinity-capture mass spectrometry identifications suggest over 150 and 229 interactors for S100A8 and S100A9 proteins, respectively (12). Expression levels of S100A8, S100A9, or both proteins change significantly with the development of many human diseases, including rheumatoid arthritis, psoriasis, ulcerative colitis, and Crohn disease, and various human cancers, including breast, prostate, pancreatic, liver, and skin cancer (1, 13, 14).

The extraordinary diversity of physiological functions of S100A8 and S100A9 has long been the subject of research. However, it is still puzzling, considering that both are small, single-domain proteins, containing only two EF-hand structural motifs connected with a short linker. According to available data, S100A8 and S100A9 have almost identical 3D structures yet perform diverse roles, depending on the biological context (15). The regulation of their function must thus rely not only on their overall static fold but also on more transient factors modulating structural dynamics, thermal stability, or susceptibility to additional factors. Theoretical studies have suggested that intertwined in the conserved S100 protein folds are sequence fragments predicted to have high intrinsic levels of disorder. A higher propensity for disorder was proposed for the sequence of S100A9 than for S100A8 (16).

S100A8 and S100A9 do not exist as monomers. They are isolated from biological samples mostly as noncovalent hetero-oligomers of S100A8 and S100A9 with 1:1 stoichiometry (17). The S100A8/S100A9 heterodimer (calprotectin) is the preferred assembly if the two recombinant proteins are cofolded *in vitro*, from denaturing conditions, for example, but it does not form upon the mixing of already folded homodimers, which are the minimal functional units for the individual proteins (18–20). Tissue-specific protein expression profiles and detailed proteomic studies indicate that relative levels of S100A8 and S100A9 *in vivo* may depart from equimolar, suggesting the significance of other biologically active complexes (21). The proteins can form higher-order oligomers that exhibit specific biological properties depending on environmental

* For correspondence: Aleksandra Wysłouch-Cieszyńska, olawyslouch@ibb.waw.pl.

conditions (22). Oligomerization of S100A8 and S100A9 is related to the binding of divalent metal ions. Each protein binds two Ca^{2+} ions in noncanonical and canonical loops located in the N- and C-terminal EF-hands (18, 20). Some proteoforms, particularly the heterodimer, also bind transition metal ions, including, Zn^{2+}, Ni^{2+}, Fe^{2+}, and Mn^{2+}, in additional sites (6, 23, 24). The oligomers differ in proteolytic stability, ligand/ion specificity, and susceptibility to posttranslational modifications (6, 25–27). For instance, S100A8/S100A9 heterodimers, released from the low-Ca^{2+} interior of cells, form tetramers in the Ca^{2+}-rich intercellular space. In psoriasis, calprotectin dimers bind to TLR4 receptors to induce inflammation signals. Tetrameric calprotectin loses this capability because the TLR4-binding epitope hides at the interface between the dimers. Thus, the localization of its dimeric form capable of TLR4 binding is focused, allowing for precise control of the spread of the inflammation signal (3). The Ca^{2+}-bound tetramer acts instead as an antibacterial agent through a "nutritional immunity" mechanism by depriving bacteria of essential transition metal ions. Strong binding of Zn^{2+}, Mn^{2+}, Ni^{2+}, and Fe^{2+} is provided by two sites formed at the heterodimer interface. The first is a classical H3D site built of the side chains of $H83_{A8}$, $H87_{A8}$, $H20_{A9}$, and $D30_{A9}$. The second is a unique H6 site involving the two imidazoles of $H17_{A8}$ and $H27_{A8}$ from S100A8 and the four imidazoles of the $H91_{A9}$, $H95_{A9}$, $H103_{A9}$, and $H105_{A9}$ residues from the S100A9 tail. Transition ion affinity drops significantly in the absence of Ca^{2+} (6, 7, 28, 29). In an excess of Zn^{2+} ions, calprotectin assembles into higher, noncanonical oligomers, leading to harmful amyloid deposits, as observed in Zn^{2+}-rich prostate cancer cells (30).

The mechanistic rationales underlying effects like heterodimerization and metal ion–dependent tetramerization are still under debate. Available structures represent primarily static data and describe only the limited, successfully crystallized conformers determined with flexible regions excluded, mainly in a metal ion–loaded form (Table S1). Remarkably, there is no structure of calprotectin in the apo form. All published structures have a similar main-chain conformation and do not clearly explain observed functional differences between oligomeric assemblies under varying conditions. Also, most crystallized proteins have their reactive cysteines ($C42_{A8}$ and $C3_{A9}$) mutated or removed, which is a disadvantage because S100A8 and S100A9 proteins are particularly susceptible to oxidative modifications *in vivo*, and the posttranslational redox modifications of methionine and cysteine residues regulate some of their biological activities (25–27, 31). A promising direction is to combine biophysical methods with computer simulations, as has been already done to study the conformational dynamics of S100A11 (32).

In this work, we applied hydrogen–deuterium exchange mass spectrometry (HDx-MS) combined with molecular dynamics (MD) simulations as a complementary technique for structural studies. We aimed to provide the missing conformational comparison of the full-length, nonmutated S100A8 and S100A9 proteins arranged in different oligomeric structures. HDx-MS has already been helpful, in our hands, in studying conformational consequences of posttranslational modifications in proteins that escape classical structure elucidation (33). A significant advantage of the method is that proteins can be analyzed without labeling and under widely varying conditions. Most importantly, HDx-MS results reflect the structural flexibility and dynamics of the investigated systems (34–36). By superimposing HDx profiles with molecular dynamic simulations, we tried to infer how the conformational characteristics of S100A8 and S100A9 subunits evolve when switching from homodimers to heterodimers, and from apo forms to Ca^{2+}- or Zn^{2+}-loaded oligomers. Eventually, we demonstrate that their properties are modulated at the level of conformational plasticity, tuned at particular protein regions in different proteoforms.

Results

Preparation and characterization of homogenous recombinant S100A8 and S100A9 oligomers

Wildtype human S100A8 and S100A9 proteins were individually overexpressed in *E. coli* and purified to homogeneity under denaturing conditions using HPLC (Fig. S1*A*). S100A8 and S100A9 complexes were obtained by refolding denatured proteins back to their native structures by dialysis from pH 2.5 to pH 7.5, as described (20). Refolded proteins assembled into either a homodimer when using pure S100A8 or S100A9 or heterodimers for an equimolar mixture of purified S100A8 and S100A9. Anion exchange chromatography and gel filtration showed that the dimers were noncovalent, and HPLC, SDS-PAGE, and liquid chromatography (LC)–electrospray ionization (ESI)–MS of whole proteins confirmed the composition of appropriate proteoforms (Fig. S1, *A*–*C*). Circular dichroism (CD) spectroscopy demonstrated the formation of the expected α-helical structures observed in these proteins previously (20, 37, 38) (Fig. S1, *D* and *E*). Size-exclusion chromatography (SEC) (Fig. 1, *A*–*C*) and analytical ultracentrifugation (Fig. 1*D*) indicated that pure S100A8 and S100A9 proteins formed only homodimers regardless of the presence of Ca^{2+}/Zn^{2+} ions. Heterodimers assembled into tetramers upon the addition of Ca^{2+} or into even higher oligomers with Zn^{2+}. According to native MS results, the predominant proteoform for S100A8/S100A9 in the presence of excess Ca^{2+}/Zn^{2+} ions remained the tetramer (Fig. 1, *E* and *F*).

Since human S100A8 and S100A9 proteins possess reduced cysteine residues, we paid special attention throughout the purification process to prevent the formation of a covalent disulfide or other oxidation product. Before each experiment, we confirmed the reduced state of cysteine thiols by HPLC and MS analysis. The redox stability of cysteines differed markedly among the various purified proteoforms. Calprotectin and $(S100A8)_2$ did not form covalent disulfide bonds in solution even after several days of storage at 4 °C without a thiol-reducing agent, while $(S100A9)_2$ had to be used immediately after purification, as it formed covalent dimers more efficiently.

Proper folding of all analyzed proteoforms was also assessed by thermal stability measurements using nanodifferential fluorescence based on tryptophan fluorescence analysis. S100A8 and S100A9 proteins have one tryptophan residue

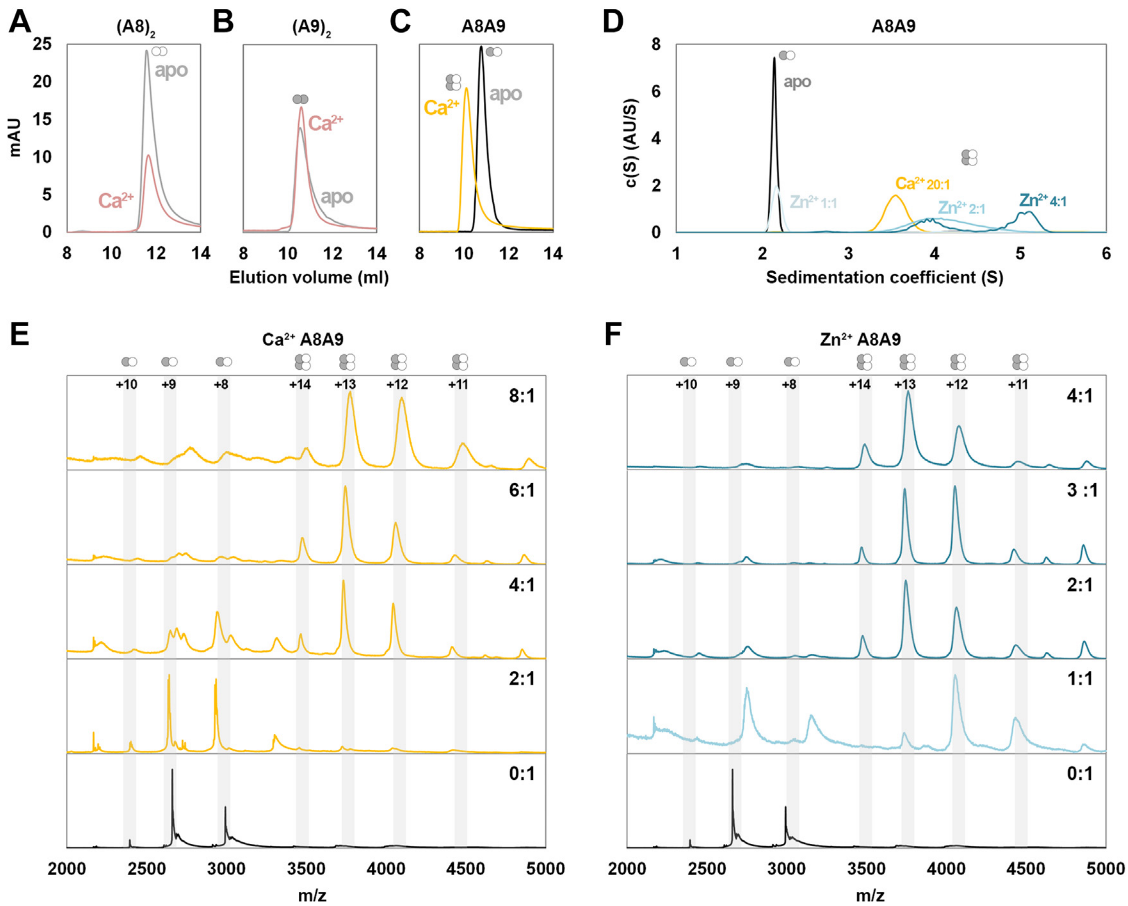

Figure 1. Oligomeric status of S100A8 and S100A9 proteins. *A–C*, size-exclusion chromatography elution profiles of 50 μM (*A*) $(S100A8)_2$, (*B*) $(S100A9)_2$, and (*C*) S100A8/S100A9 in the absence (*gray* or *black line*) and presence of 1 mM Ca^{2+} (*pink* or *yellow line*). Elution buffer: 20 mM TES pH 7.5, 100 mM NaCl, ± 1 mM Ca^{2+}; 20 °C. *D*, sedimentation coefficient distributions for 25 μM S100A8/S100A9 in the absence (*black line*) and presence of 500 μM Ca^{2+} (*yellow line*), 25 μM Zn^{2+} (*light blue line*), 50 μM Zn^{2+} (*blue line*), and 100 μM Zn^{2+} (*dark blue line*). *E* and *F*, native mass spectrometry spectra of 25 μM S100A8/S100A9 in the absence and presence of (*E*) Ca^{2+} ions with the metal:protein stoichiometries 2:1, 4:1, 6:1, and 8:1, and (*F*) Zn^{2+} ions with the metal:protein stoichiometries 1:1, 2:1, 3:1, and 4:1. Each mass spectrum was normalized to a maximum peak value of 1. The pseudomolecular ion charges are provided above the corresponding peaks.

each. In homodimers at room temperature, $W88_{A9}$ is more exposed to the solvent (fluorescence at 350 nm/330 nm [F] = 0.94) than is $W54_{A8}$ (F = 0.74). The F value for Trp fluorescence in the heterodimer is an arithmetic mean of the values obtained for the homodimers (F = 0.84). Upon Ca^{2+}-induced tetramerization, the Trp fluorescence drops (F = 0.71), indicating an additional burial of Trp side chains. With increasing temperature, the tryptophans in $(S100A8)_2$ become buried (red shifted in fluorescence), while in $(S100A9)_2$ and calprotectin they become exposed (blue shifted). The observed unfolding transitions were sudden and occurred at quite different temperatures. Calprotectin showed much higher stability ($T_m[A8A9^{apo}]$ = 70.2 °C, $T_m[A8A9^{Ca2+}] \approx 75$ °C) compared with homodimers ($T_m[A8^{apo}] = T_m[A8^{Ca2+}] \approx 60.5$ °C, $T_m[A9^{apo}] = T_m[A9^{Ca2+}] \approx 61.7$ °C) (Fig. S1*F*).

Hydrogen–deuterium exchange mass spectrometry for S100A8 and S100A9 proteins

We performed HDx-MS experiments to gain insight into the conformational dynamics of the homogenous S100A8 and S100A9 oligomers. Using tandem mass spectrometry, we observed that digestion of each studied proteoform by pepsin at pH 2.5 yielded, among others, 39 peptides from the S100A8 subunit and 49 from S100A9, altogether covering 93% of the proteins (Fig. 2 and Table S2). Only two fragments from the N termini of helices IV ($A8_{69–74}$ and $A9_{79–83}$) could not be detected. Despite minor differences between our protocols (see Experimental procedures) and those previously reported in the literature for a Cys/Ser mutant of calprotectin (39), the digestion results remained consistent, with only a slightly decreased number of obtained peptides (39 *versus* 40 for S100A8, and 49 *versus* 55 for S100A9, Table S2). We measured the deuterium uptake levels for the same sets of peptides in each proteoform at five exchange time points: immediately after D_2O addition and at 10 s, 1 min, 5 min, and 24 h of HDx.

$(S100A8)_2$ and $(S100A9)_2$ homodimers

HDx-MS for apo homodimers demonstrated substantial differences in deuteration levels between $(S100A8)_2$ and $(S100A9)_2$. The HDx profile for apo $(S100A8)_2$ consists of alternating regions characterized by lower and higher deuterium uptake that correlate well with the localization of α-helices (Figs. 3*A* and S2). Less protected fragments correspond to the loose parts, such as the protein's termini, Ca^{2+}-binding

Figure 2. Sequence coverage map of identified peptic peptides obtained for S100A8 and S100A9 proteins.

loops, and linker between the two EF-hand motifs. While the exchange levels eventually saturated after 5 min for most of the protein sequence, the peptides from helix I (*i.e.*, $A8_{5-15}$) remained barely accessible to the solvent. For $(S100A9)_2$, HDx levels were much less differentiated (Figs. 3*B* and S3), and the regions within α-helices not as pronounced. The only peptide with low (<25%) deuterium uptake after 10 s derives from helix I ($A9_{14-19}$) and corresponds to the most protected fragment in $(S100A8)_2$. Yet, in contrast to $(S100A8)_2$, after 1 and 5 min of exchange, the exchange rates for this peptide reached 60% and 90%, respectively. Also, helices II and IV were more protected in $(S100A8)_2$ than in $(S100A9)_2$ (∼30% *versus* ∼55%, and 45% *versus* 80% at the 10-s time point, respectively). Conversely, the Ca^{2+}-binding loops are more dynamic in $(S100A8)_2$ (80%–100% after 10 s) as compared with the loops in $(S100A9)_2$ (∼70%).

$(S100A8)_2$ and $(S100A9)_2$ homodimers upon Ca^{2+} binding

In both homodimers, the binding of calcium stabilizes the Ca^{2+}-binding loops only slightly, with the most pronounced effect on the canonical loop in $(S100A9)_2$. There are, however, also substantial differences. $(S100A8)_2$ becomes less dynamic mainly within helix II, and this is clearly pronounced for the peptide $A8_{31-39}$ at all measured times (Figs. 4, *A* and *C* and S2). In $(S100A9)_2$, on the other hand, the HDx profile deviated substantially, becoming differentiated between the more protected helices I, II, and III and the less protected linker and helix IV (Figs. 4*B* and S3). After 5 min, both profiles converged back to resemble their apo counterparts. Only helices I and II remained more protected, especially in $(S100A8)_2$ (Fig 4, *C* and *D*), and the C terminus of $(S100A9)_2$ remained less protected.

Apo S100A8/S100A9 heterodimer

Heterodimerization had an even more profound effect on HDx dynamics in each protein compared with either apo or Ca^{2+}-loaded homodimers. In the S100A8 subunit, helices I and II and the linker became further protected, increasing the contrast with the accessible Ca^{2+}-binding loops and helix III. Despite the overall protein stabilization, helix IV experienced increased exchange rates relative to the homodimer (Figs. S2 and S3). S100A9 displayed an overall significant decrease in

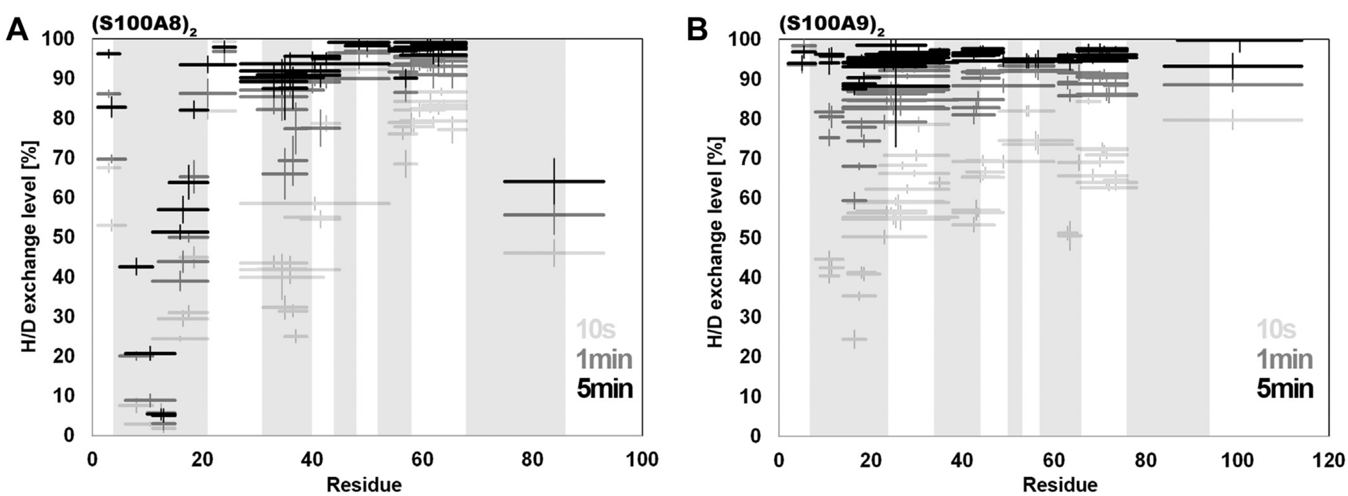

Figure 3. Hydrogen–deuterium exchange levels resolved to individual peptide segments in apo homodimers. The measurements were made at three different time points for (*A*) $(S100A8)_2$ and (*B*) $(S100A9)_2$.

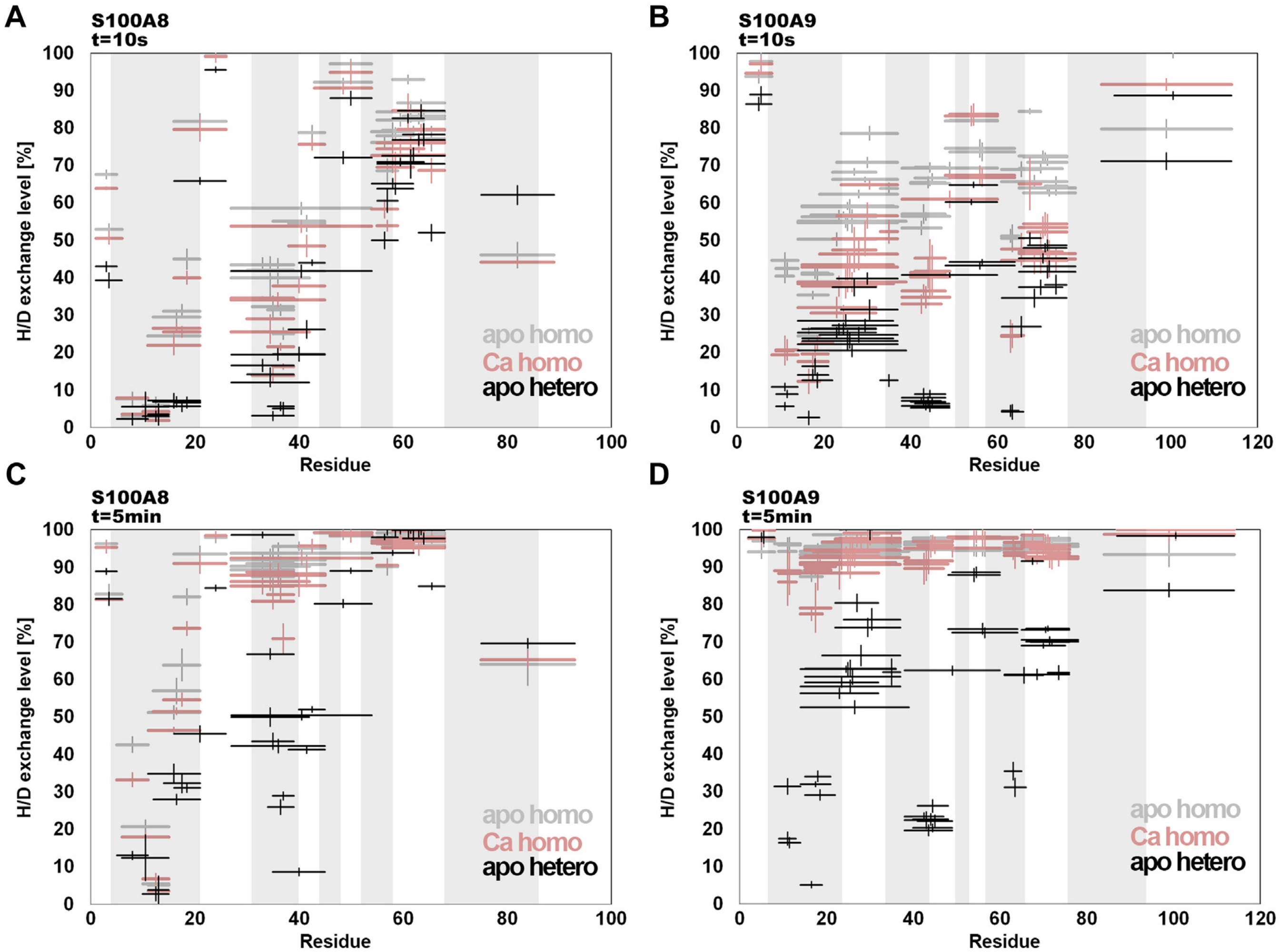

Figure 4. Hydrogen–deuterium exchange levels for apo and Ca^{2+}-loaded homodimers, and apo heterodimers. The measurements were made after 10 s in (*A*) $(S100A8)_2$ and (*B*) $(S100A9)_2$ and after 5 min in (*C*) $(S100A8)_2$ and (*D*) $(S100A9)_2$.

HDx levels, especially for helices I, II, and III within the linker; helix IV; and the Ca^{2+}-binding loops. In contrast to the homodimers, the HDx profiles of the subunits in heterodimers retained definition even after 5 min of exchange, and their HDx profiles became more alike. Notably, heterodimerization in the absence of metal ions decreased deuterium uptake by both Ca^{2+}-binding loops in S100A9. The loop protection was higher than after Ca^{2+} addition to the homodimers (Fig. 4*B*), especially after 5 min of exchange (Fig. 4*D*).

Ca^{2+}-induced tetramerization of the S100A8/S100A9 heterodimer

Loading calprotectin with Ca^{2+} ions promoted further decline in HDx ratios in both subunits. Now the last core structural element, helix III, became protected (Fig. 5, *A* and *B*). This effect was already pronounced for S100A9 in the apo heterodimer, but here it became apparent for both proteins. The canonical loops also showed substantially less exchange. This is in contrast to the small effect of Ca^{2+} binding on the same loops in homodimers but consistent with the data from the Ser/Cys calprotectin mutant (Fig. 5*C*). In conclusion, in the Ca^{2+}-bound calprotectin tetramer, helices I, II, and III are almost inaccessible for HDx, while the noncanonical loops and C-terminal parts remain flexible (Figs. S2 and S3).

Zn^{2+}-induced tetramerization of S100A8/S100A9 heterodimer

The transition metal ion Zn^{2+} has different binding-site preferences than the alkali-earth metal ion Ca^{2+} (6). However, Zn^{2+}-induced changes in HDx levels for both S100A8 and S100A9 had the exact localization, direction, magnitudes, and even kinetics of Ca^{2+}-bound calprotectin (Figs. 5, *D–F*, S4 and S5). A Zn^{2+}-specific decrease in deuterium uptake (by 25%–40%) could be observed only for peptides containing residues directly involved in the coordination of Zn^{2+} ions: $A8_{16–26}$, $A8_{75–93}$, $A9_{22–32}$, and $A9_{87–114}$. The binding of additional Zn^{2+} ions to the already Ca^{2+}-loaded tetramer did not affect its HDx profile, except for lowering HDx at the Zn^{2+}-binding sites and in the S100A9 noncanonical loop ($A9_{23–37}$, change from 80% to 30%) (Figs. 5, *D* and *E* and S8).

Notably, for longer D_2O incubation times, specifically in the absence of Ca^{2+}, but in one or two molar Zn^{2+} excess, double envelopes (Fig. S9) of differing intensities could be observed for most calprotectin peptides, leading to enhanced

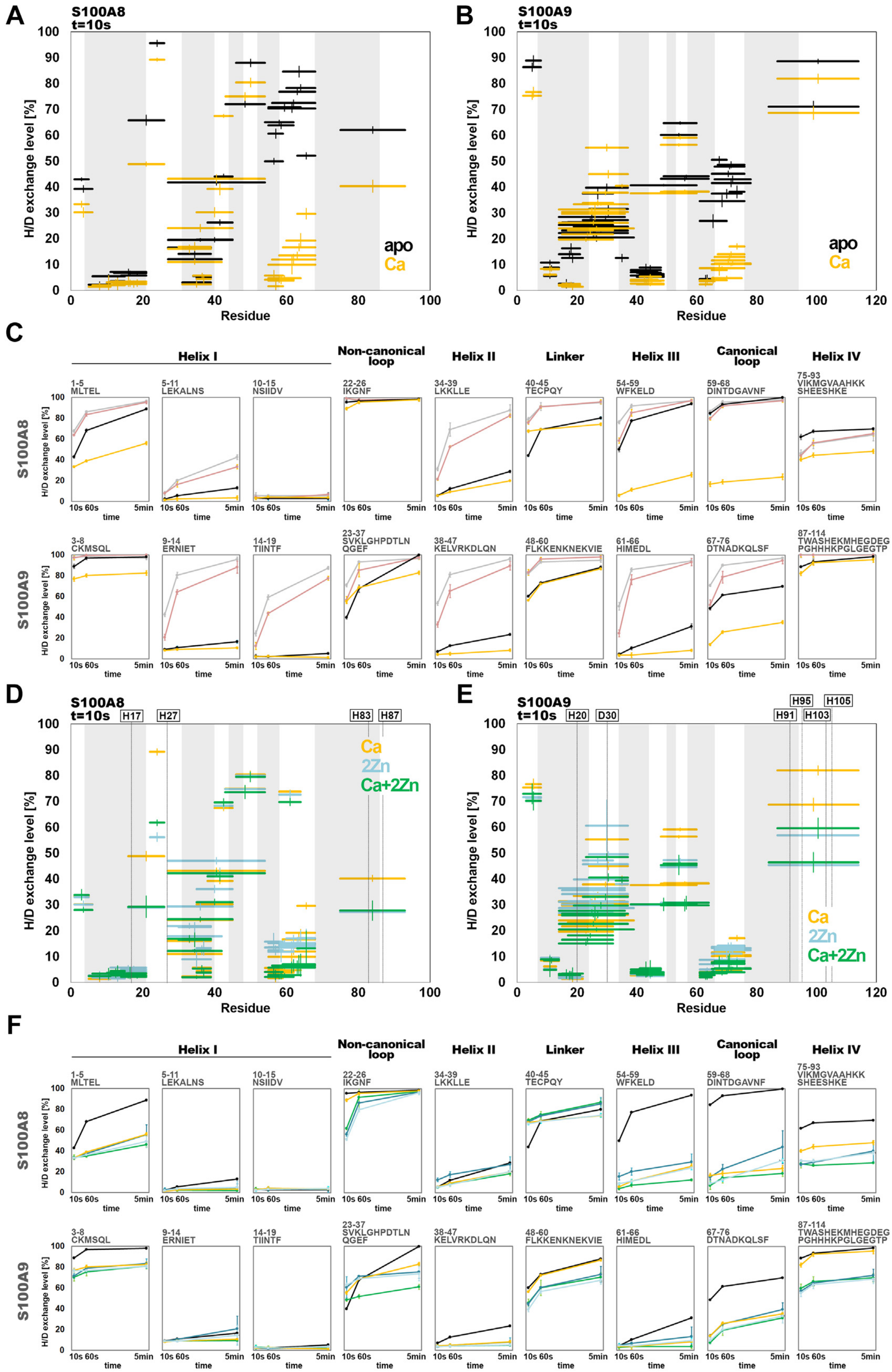

Figure 5. Comparison of hydrogen–deuterium exchange (HDx)–mass spectrometry results for S100A8/S100A9 heterodimer. HDx levels after 10 s in (*A*) S100A8 and (*B*) S100A9 within apo and Ca^{2+}-loaded heterocomplexes; (*C*) HDx levels for chosen peptides representing major structural elements of S100A8 and S100A9 within homo- and hetero-oligomers in the absence (grey and black, respectively) and presence of Ca^{2+}(yellow and pink, respectively); HDx levels after 10 s in (*D*) S100A8 and (*E*) S100A9 within heterocomplexes after 10 s measured with and without 1- or 2-molar excess of Zn^{2+} ions; (*F*) HDx levels for chosen peptides representing major structural elements of S100A8/S100A9 after 10 s, 1 min, and 5 min of exchange in the absence (black) and presence of Ca^{2+} (yellow), 1-molar (blue) or 2-molar (light blue) excess of Zn^{2+}.

measurement errors. Such an effect is consistent with the analytical ultracentrifugation data suggesting significant oligomerization heterogeneity.

Comparison of Ca^{2+}- versus Zn^{2+}-induced oligomerization

To compare the effects of Ca^{2+} or Zn^{2+} binding and tetramerization on calprotectin conformational dynamics, we measured HDx levels for individual peptic peptides along the S100A8 and S100A9 sequences upon titration with Ca^{2+} or Zn^{2+} ions. This approach is a so-called protein–ligand interaction in solution by mass spectrometry, titration, and hydrogen/deuterium exchange (PLIMSTEX) experiment. The PLIMSTEX approach recently provided data quantifying Ca^{2+} binding to mutant Cys/Ser calprotectin (39). Upon Ca^{2+} titration in the PLIMSTEX experiment, HDx levels initially stayed constant for most peptides until the Ca^{2+}:protein ratio reached 5:1, subsequently decreasing and eventually stabilizing at the Ca^{2+}:protein ratio of 10:1 (Figs. 6*B*, S6 and S7). Consistent with the results related to HDx levels presented above, the canonical Ca^{2+}-binding loops from both subunits presented the most pronounced decrease in HDx levels (on average, from 100% to 30% in S100A8 and from 70% to 45% in S100A9), compared with helices III_{A8} and IV_{A8} (~70%–45%) and helix I_{A9} (20%–3%). The noncanonical loop from S100A8 remained insensitive to Ca^{2+} concentration. Similar effects were observed for Zn^{2+} titration, with changes occurring between the ratios of 0.5:1 and 1.25:1. Unlike with Ca^{2+}, in this case, helix $IV_{A9,}$ which hosts histidines for Zn^{2+} binding within the H6 site, was also stabilized.

Three regions of calprotectin displayed the most apparent changes in HDx levels upon tetramer association, namely, helix III_{A8} and the canonical Ca^{2+} loops in both subunits (Fig. 6*A*). Figure 6*B* additionally shows that peptic peptides covering these protein regions could be assigned to two separate isotopic envelopes, indicating two stable conformations for the metal-ion loaded and unloaded proteoforms (peptides marked with red asterisks). Helix III_{A8} and the canonical loop of S100A9 settled into one conformation at a Ca^{2+}:protein ratio of 5:1, but the canonical loop of S100A8 continued to display dual characteristics even up to a 50:1 excess of Ca^{2+} ions. Double isotopic envelopes for these peptides were also observed in Zn^{2+}-induced tetramerization (Fig. 6*C*); however, the effect did not diminish even in higher ion excess. Similar to what was observed for Ca^{2+} titration, the canonical loop of S100A8 remained least stabilized within its final conformation and kept switching between two states at the ratio of 0.66:0.34 (Fig. 6*D*).

Molecular dynamics simulations

To gain more mechanistic insight into the dynamics reflected in HDx results reported above, we performed MD simulations for all the proteoforms. As a starting point, we used structures available in the Protein Data Bank (PDB) database. If a proteoform had been studied only with Ca^{2+} ions, we used its structure and removed the ions before the simulation run for an apo protein (*e.g.*, $(S100A8)_2$ - pdb|1mr8, S100A8/S100A9 - pdb|4ggf). We ran MD for the calprotectin tetramer without ions to double-check whether deleting ions from the X-ray structure would affect the simulation results. The tetramer disassembled into two dimers after less than 50 ns of simulation time, as expected since tetramers are known to form only in conditions of ion excess. We added Ca^{2+} ions before calculations for Ca^{2+}-loaded simulation if the only available structure lacked them (*e.g.*, $[S100A9]_2$ - pdb|5i8n). We also reverted the Cys/Ser mutations when present. Although MD simulations cover a much shorter timescale than HDx experiments (at most 500 ns *versus* 10 s), the results were consistent enough to draw rational conclusions. We present the overall flexibility of the subunits calculated in MD simulations as a comparison of the root-mean-square fluctuations (RMSFs) for S100A8 and S100A9 in different proteoforms (Fig. S10).

The MD results for both homodimers in apo form immediately demonstrated the higher stability of $(S100A8)_2$ compared with $(S100A9)_2$ (Fig. 7, *A* and *B*). The distances between helices I_{A8} were more rigid in $(S100A8)_2$ as measured for $V15_{A8}$-$L5_{A8}$ and $A8_{A8}$-$A8_{A8}$ and their counterparts in $(S100A9)_2$, $L8_{A9}$-$T18_{A9}$ and $N11_{A9}$-$N11_{A9}$. Similarly, increased $(S100A8)_2$ helix IV_{A8} protection correlated with the distance $G79_{A8}$-$L9_{A8}$ (Fig. 7*C*), which was more stable than $T87_{A9}$-$I12_{A9}$ (Fig. 7*D*). The observed differences are probably a consequence of the better packing of more hydrophobic residues lining the interhelical interfaces in $(S100A8)_2$. Helix II_{A8}, in turn, seems to be stabilized in $(S100A8)_2$ by ionic bonds $D33_{A8}$-$K23_{A8}$ and $E41_{A8}$-$K18_{A8}$. In $(S100A9)_2$, the corresponding pairs $E36_{A9}$-$K25_{A9}$ and $D44_{A9}$-$Q21_{A9}$ remained disconnected, the latter apparently due to the different properties of the residues involved (glutamic acid *versus* glutamine).

Ca^{2+}-binding loops, unlike the core parts of the homodimer, remained less stable in $(S100A8)_2$ compared with $(S100A9)_2$ (Fig. 8). An extensive network of bonds between $D67_{A9}$ and amides lining the canonical loop was maintained more rigidly than its counterpart, $D58_{A8}$. Moreover, although in all S100 proteins a short β-sheet forms between the canonical and noncanonical loops, it is longer and more pronounced in $(S100A9)_2$, where it is stabilized by two hydrogen bonds between $L74_{A9}$-$L32_{A9}$ and $P29_{A9}$-$F76_{A9}$ (Fig. 8*C*). Also, $P29_{A9}$ defines an apex of this β-sheet by imposing conformational constraints that may additionally contribute to local stability. In $(S100A8)_2$, the β-sheet disassembles and the loops become disentangled.

Upon heterodimer formation, additional interactions emerge that correspond to the stabilization of helices I and II observed in HDx profiles for both subunits. Helices I are linked by the $S11_{A8}$-$N11_{A9}$ interaction (Fig. 9*A*), the most stabilizing factor in this calprotectin region. There is no candidate for a similar interaction in homodimers. The N terminus of helix I_{A9} becomes more stable than it is in the homodimer. The $E41_{A8}$ carboxylate moiety, although located in the proximity of the $K18_{A8}$ side chain and amide of $L8_{A9}$, seems to have only a minor impact on the dynamics of this region and either does not set up stable interactions at all or forms them only occasionally. Also, $Q7_{A9}$-$S11_{A8}$ and $Q7_{A9}$-$K18_{A8}$ interactions,

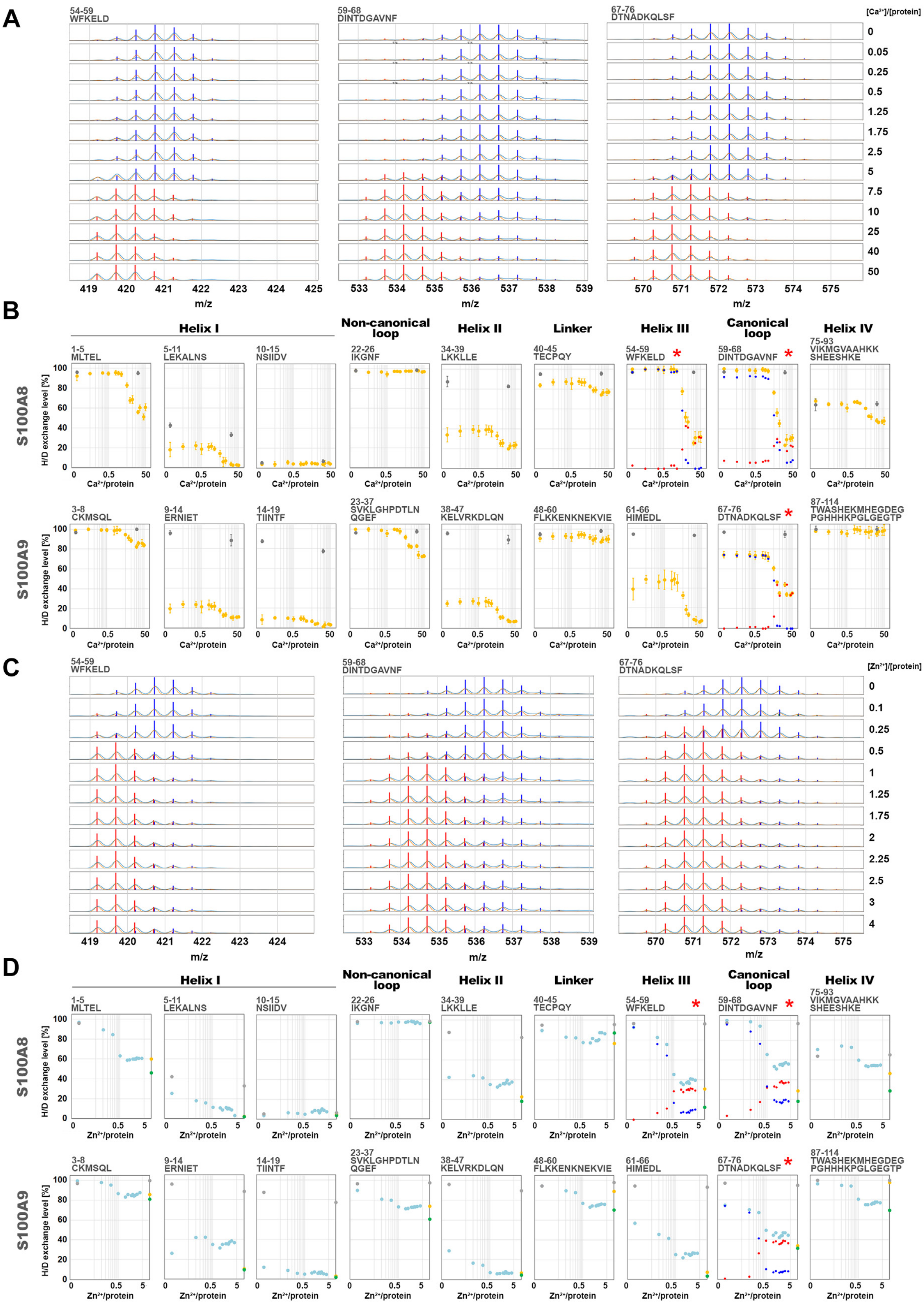

Figure 6. PLIMSTEX titrations of apo calprotectin with Ca^{2+} and Zn^{2+} ions (*orange or blue dots*, respectively). Double isotopic envelopes assigned to peptides $A8_{54–59}$, $A8_{59–68}$, and $A9_{67–76}$ (marked with *red stars*) during titration with (*A*) Ca^{2+} and (*C*) Zn^{2+}. Hydrogen–deuterium exchange levels measured after 5 min of exchange as a function of (*B*) Ca^{2+} and (*D*) Zn^{2+} ion concentration. For each peptide, *gray dots* represent the exchange levels measured under the same conditions for apo and for Ca^{2+}-bound homodimers and hetero-oligomers. *Red* and *blue dots* indicate hydrogen–deuterium exchange levels for two observed conformers. The PLIMSTEX results for Zn^{2+} titrations of Ca^{2+}-devoid calprotectin varied substantially between biological replicates, and a

although clearly defined in the calprotectin X-ray structure, are not maintained in the simulations. On the opposite end of helix I_{A9}, an essential role in heterodimer stabilization is played by $Y22_{A9}$ (Fig. 9*B*). $Y22_{A9}$-$D44_{A9}$, $D44_{A9}$-$T3_{A8}$, and $E6_{A8}$-$N47_{A9}$ form a rigid network of hydrogen bonds consistent with the observed substantial HDx decrease here (30% for S100A8 and >60% for S100A9). However, in $(S100A9)_2$, the tyrosine phenol flips to interact with the side chains of either $D44_{A9}$ or $S6_{A9}$, which disrupts surrounding interactions (Fig. 9*C*). Finally, the increased stability of the C terminus of helix IV_{A9} is a consequence of the emerging $N10_{A8}$-$S90_{A9}$ interaction.

Upon Ca^{2+} binding, $N10_{A8}$-$S90_{A8}$ and $S11_{A8}$-$Q7_{A9}$ become more stable (0.28 ± 0.03 nm *versus* 0.42 ± 0.24 nm for apo and 0.41 ± 0.11 nm *versus* 0.58 ± 0.29 nm for apo, respectively) and contribute to a further increase in instability of the N-terminal EF-hand domains within calprotectin dimers, as observed in HDx.

According to crystal structures of Ca^{2+}-loaded calprotectin, the dimers are fastened by Ca^{2+}-binding loops interacting at two opposite tetramer poles. Both canonical loops constitute the core of the assembly within each site, while noncanonical loops remain peripheral (Fig. 10*A*). $T68_{A9}$-$D63_{A8}$ and $E77_{A9}$-$N61_{A8}$ interactions between canonical loops were the most stable observed of all performed simulations. These interactions diminished in a control MD simulation run for tetrameric calprotectin devoid of Ca^{2+} ions (data not shown). At the interface between helices III (Fig. 10*B*), another stabilizing interaction occurs between glutamic acids $E57_{A8}$. Although in all available PDB structures of calprotectin the $E57_{A8}$ residue interacts with either lysine $K49_{A8}$ (pdb|6ds2, pdb|1xk4) or lysine $K77_{A8}$ (pdb|5w1f), none of these interactions is stable according to the MD results. Instead, the distance between a pair of $E57_{A8}$ side chains from two interacting heterodimers seems to be maintained through the intermediation of several water molecules (Fig. 10*B* inset).

Besides the peripheral regions of interacting loops, the central part of an interface between calprotectin dimers forms an empty pocket hosting, for example, $W88_{A9}$ residues. According to MD simulations this space continues to be accessible to solvent, which raises the question of the drop in $W88_{A9}$ fluorescence upon tetramerization. The dynamic behavior of residues lining the pocket's entry may explain this phenomenon. $R85_{A9}$ from helix IV_{A9} continuously switches between interaction with $D65_{A9}$ in the same dimer and $E92_{A9}$ incoming from the other dimer, acting like a windshield wiper and limiting access to the pocket (Fig. 11). Moreover, the $E92_{A9}$-$R85_{A9}$ interaction also stabilizes the tetramer.

Formation of the proposed pocket may be the cause of changes in the characteristic tryptophan-related chirality at 285 to 300 nm observed in the near-UV circular dichroism spectra in the presence of Ca^{2+} or Zn^{2+} ions in calprotectin solutions (Fig. S11). The near-UV CD spectra are close for apo homo- and heterodimers (Fig. S11*D*) but differ from those of the similar Ca^{2+} or Zn^{2+} bound tetramers (Fig. S11, *A* and *B*).

Zn^{2+} ions bind to calprotectin away from the Ca^{2+}-binding loops. There are two major Zn^{2+}-binding sites. The first is in the immediate proximity of either the S100A9 or S100A8 noncanonical loops (Fig. 10*A*). The former is lined with histidines incoming from helix I_{A9} and helix IV_{A8} and also engages $D30_{A9}$ from the noncanonical loop. Zn^{2+} binding in this place flips the $D30_{A9}$ side chain toward an ion to bind it firmly, stabilizing the loop. Ca^{2+}-binding loops are entangled in S100A9 through the short β-sheet. Thus, effects imposed on one of them are likely to affect the other, hence the enhanced stability of the S100A9 canonical loop in the presence of Zn^{2+} (Fig. 10*A*). A less dynamic canonical loop might, in turn, be more accepting of more lasting interactions with incoming S100A8. The other Zn^{2+}-binding site, the "H-6 site," is located under the S100A8 noncanonical loop, between helix I_{A8} and helix IV_{A9}. Unlike the S100A9 loops, the presence of Zn^{2+} in this site does not significantly affect the S100A8 canonical loop, and the eventual consequences for calprotectin dynamics are much harder to interpret.

Discussion

This work is a systematic comparative analysis of the wild-type human S100A8 and S100A9 proteins in different noncovalent oligomeric variants. We show that subunits exhibit substantially different conformational dynamics depending on the oligomeric state, manifested in timescales ranging from nanoseconds (in MD simulations) to minutes (in HDx-MS experiments).

A combination of HDx-MS and MD simulations reproduced well most of the interactions proposed in the static X-ray structure of Ca^{2+}-bound tetramer. Hence, we assume that our experiments also reflect the native state features for other proteoforms. For instance, the $(S100A8)_2$ homodimer maintains more rigid interaction between helices I_{A8}, the noncanonical loop, and helix II_{A8}, and between helices I_{A8} and IV_{A8}, all reflected in its HDx profile displaying regions of increased protection (helices I_{A8}, II_{A8}, and IV_{A8}). Ca^{2+} binding only slightly exaggerates the already-observed characteristics, demonstrating that $(S100A8)_2$ comes inherently preformed for ion binding. In contrast, apo $(S100A9)_2$ shows much flatter HDx ratios, which differentiate upon binding incoming Ca^{2+} ions. The structure of $(S100A9)_2$ is more malleable and adjusts its dynamical properties according to the context. Besides helix I_{A8}, both HDx profiles saturate after 5 min, even in the presence of Ca^{2+} ions. More pronounced effects emerge upon the formation of the heterodimer. Additional interactions occur between helices I_{A8} ($S11_{A8}$-$N11_{A9}$), helices I_{A8} and II_{A8} ($K18_{A8}$-$E41_{A8}$), and helices I_{A8} and IV_{A9} ($N10_{A8}$-$S90_{A9}$), and in the region between helices I_{A9} and helix III_{A9} ($Y22_{A9}$-$D44_{A9}$, $D44_{A9}$-$T3_{A8}$, $E6_{A8}$-$N47_{A9}$). HDx characteristics for both proteins became more alike and

single representative experiment of three technical replications is presented. PLIMSTEX, protein–ligand interaction in solution by mass spectrometry, titration, and hydrogen/deuterium exchange.

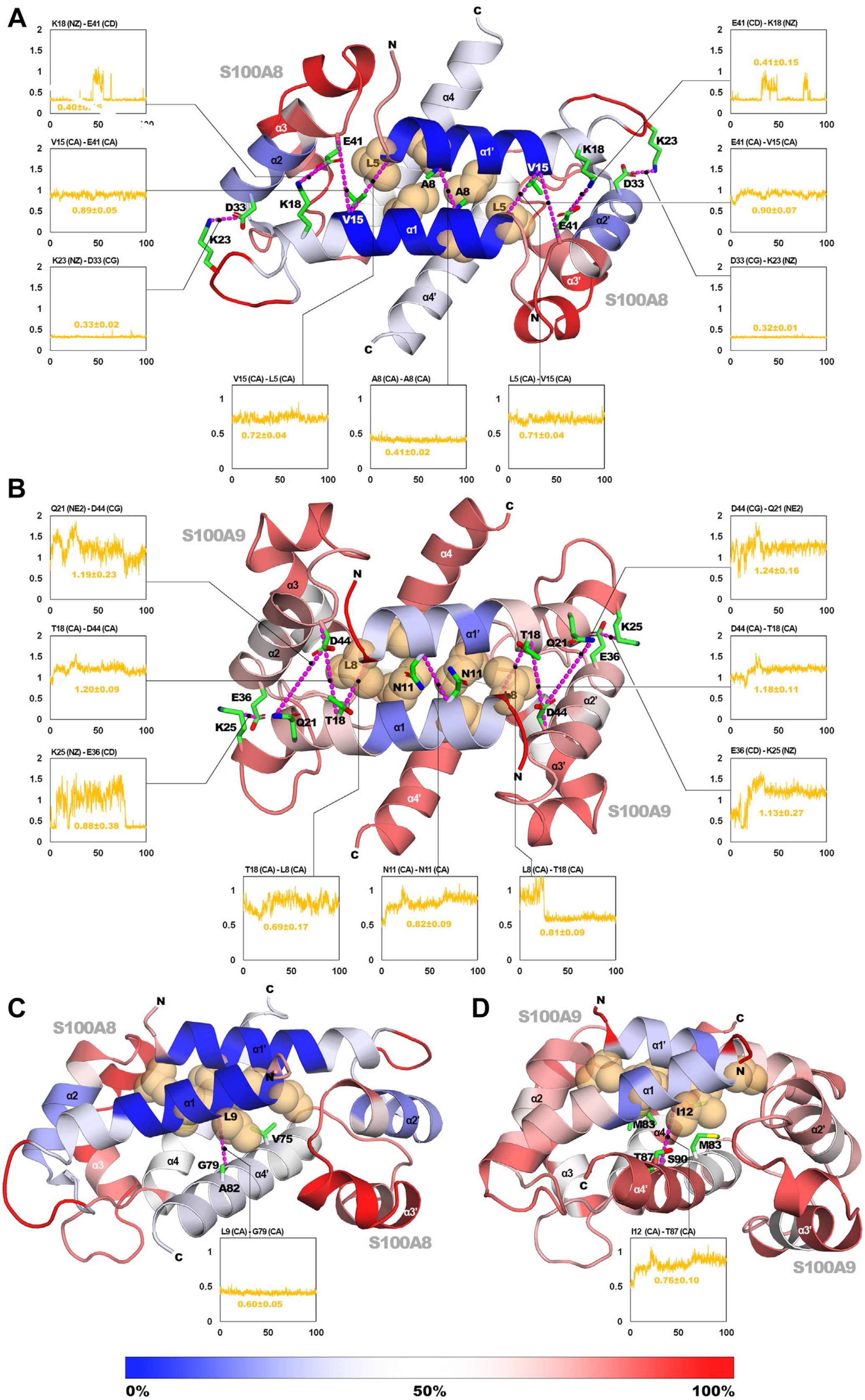

Figure 7. Dynamical properties of $(S100A8)_2$ and $(S100A9)_2$ derived from molecular dynamics simulations. Interactions between helices I in (*A*) $(S100A8)_2$ and (*B*) $(S100A9)_2$. Interaction between helices I and IV in (*C*) $(S100A8)_2$ and (*D*) $(S100A9)_2$. Residues likely contributing to the observed differences are shown with *sticks*. The plots depict the evolution of corresponding distances in molecular dynamics trajectories (the vertical axis presents the distance in nanometers *versus* time in nanoseconds on the horizontal axis). Colors on the protein structures correspond to the hydrogen–deuterium exchange levels measured after 10 s, and the coloring scale is given at the bottom.

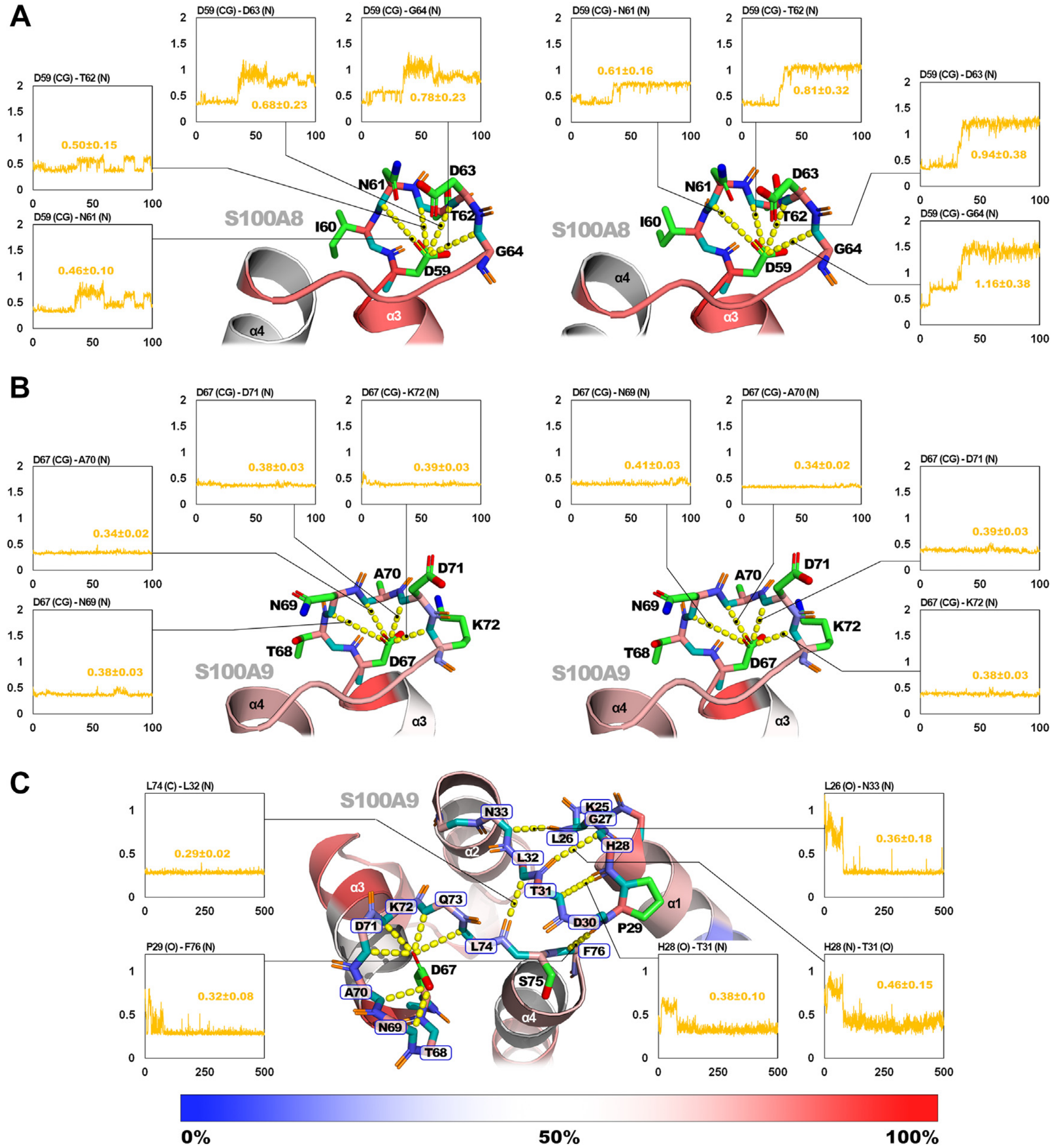

Figure 8. Interactions within canonical Ca^{2+}-binding loop. (*A*) $(S100A8)_2$ and (*B*) $(S100A9)_2$ loops display different dynamical properties according to the distances measured through MD simulation. Colors on the structures correspond to the HDx levels measured after 10 s with a coloring scale as in Figure 1. (*C*) Interactions within noncanonical Ca^{2+}-binding loop in $(S100A9)_2$.

stable even after 5 min. Eventually, tetrameric calprotectin forms in the presence of Ca^{2+} ions and the canonical loops and helices gain even more protection.

Since there is no known structure of calprotectin without Ca^{2+} ions, it was challenging to reconstruct the steps of tetramer formation and distill factors contributing to this process. Two stabilizing interactions emerge here. The first one, between the S100A8 and S100A9 canonical loops (T68$_{A9}$-D63$_{A8}$ and E77$_{A9}$-N61$_{A8}$), is highly stable. As already proposed based on the crystal structures, it is likely the primary fastener holding the dimers within the tetramer in the presence of ions stabilizing the canonical loops (15, 20). The second spans helices III$_{A8}$ between both dimers (E57$_{A8}$-E57$_{A8}$) through a network of water molecules. Both interactions clearly modify the HDx profiles and exchange kinetics. The canonical loops and helices III remain extensively protected in time. Interestingly, the noncanonical loops and C-terminal parts of the subunits remain continuously exposed to the solvent and probably provide some flexibility at transition metal–binding sites nearby.

The HDx results for canonical loops and helix III$_{A8}$ suggest the existence of two alternating conformations of the structures. In the presence of a sufficient excess of Ca^{2+} ions (>10:1), helix III$_{A8}$ and the canonical loop from S100A9 settle in a stable conformation while the remaining canonical loop in S100A8 continues to switch between two states. Unfortunately, we could not capture those conformations from the MD runs.

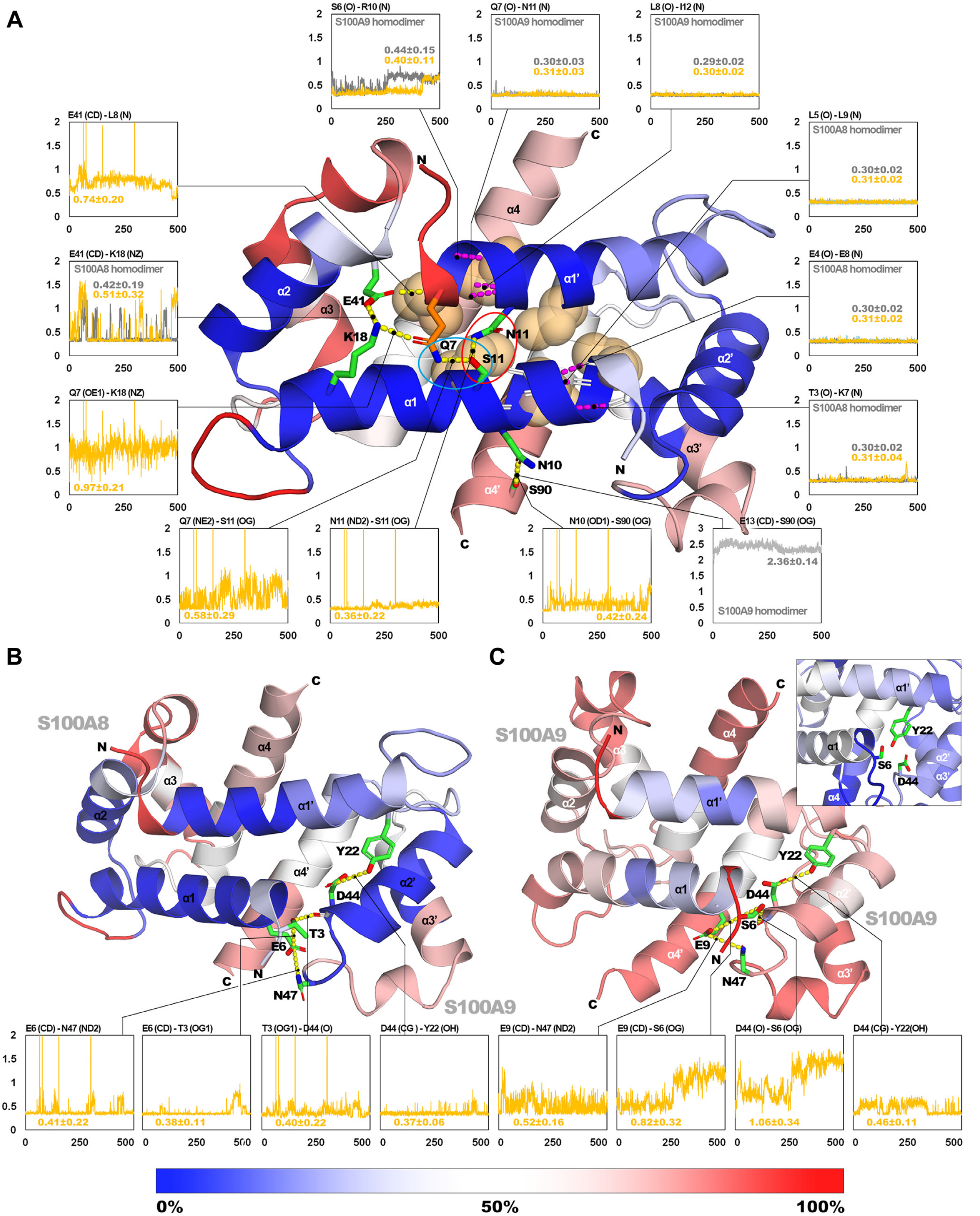

Figure 9. Comparison of hydrogen–deuterium exchange (HDx)–mass spectrometry results for calprotectin and $(S100A9)_2$ homodimer. (*A*) Stabilizing interactions in the apo calprotectin derived from MD runs. (*B*) Interaction network between $Y22_{A9}$-$D44_{A9}$, $D44_{A9}$-$T3_{A8}$, and $E6_{A8}$-$N47_{A9}$ stabilize helices I_{A9} and II_{A9} in calprotectin. In $(S100A9)_2$, these interactions dissipate while $Y22_{A9}$ fluctuates towards $S6_{A9}$, which disrupts local stability (inlet) (*C*).

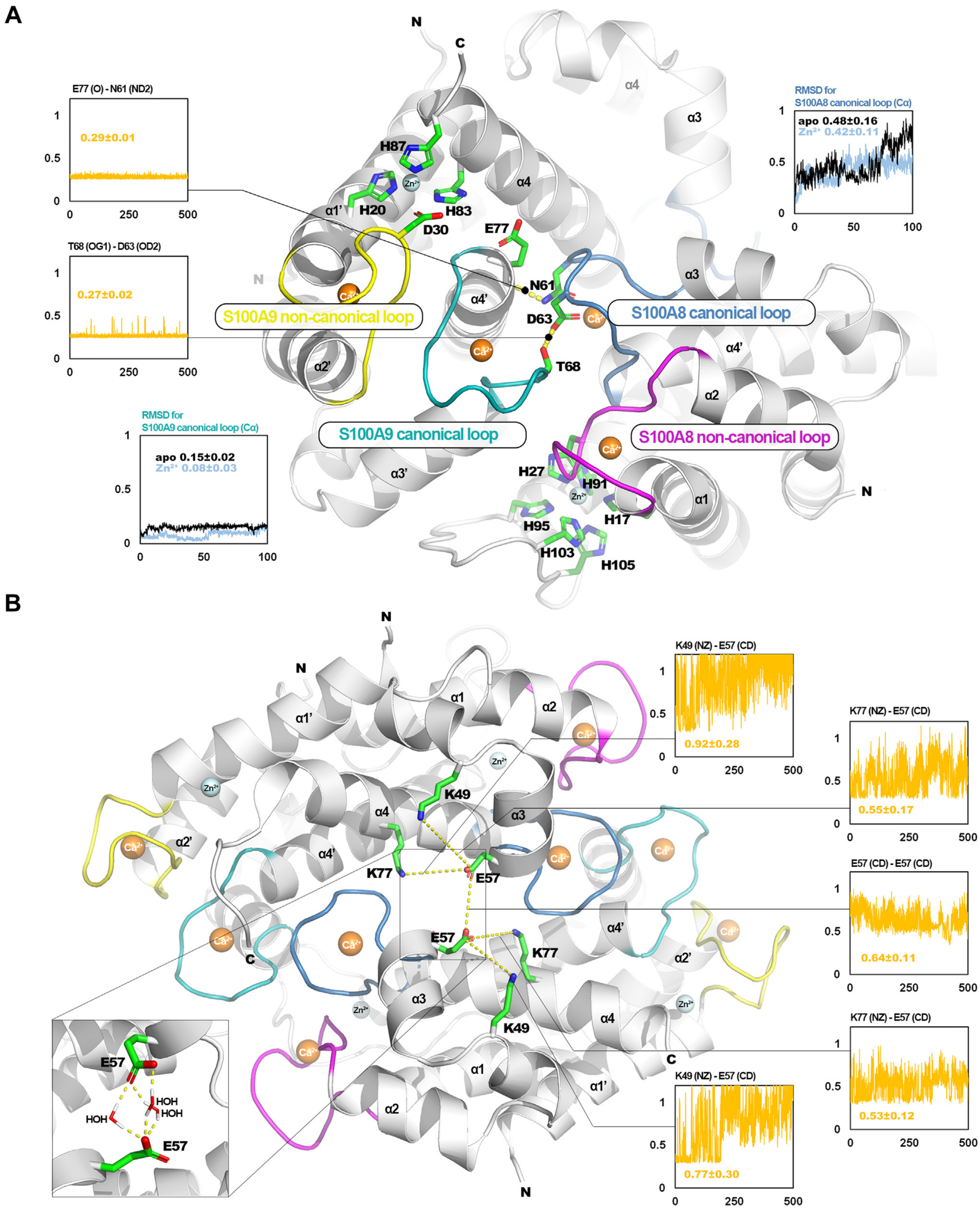

Figure 10. Interactions between heterodimers in the tetramer. *A*, Ca^{2+}-binding loops assemble and form an interface holding heterodimers together. *B*, helices III_{A8} are close to each other in a tetramer and bound by water-mediated interactions between $E57_{A8}$ residues.

The flexibility of proteins' amino termini regulates their proteolytic stability (7, 28). Indeed, the observed decline in HDx levels when comparing homodimers to heterodimer to Ca^{2+}-loaded calprotectin is pronounced at the N termini. It correlates with the previously reported increase of proteolytic resistance ($A9_2<A9_2^{Ca2+}\leq A8_2<A8_2^{Ca2+}<[A8A9]_2<[A8A9]_2^{Ca2+}$) (40) and

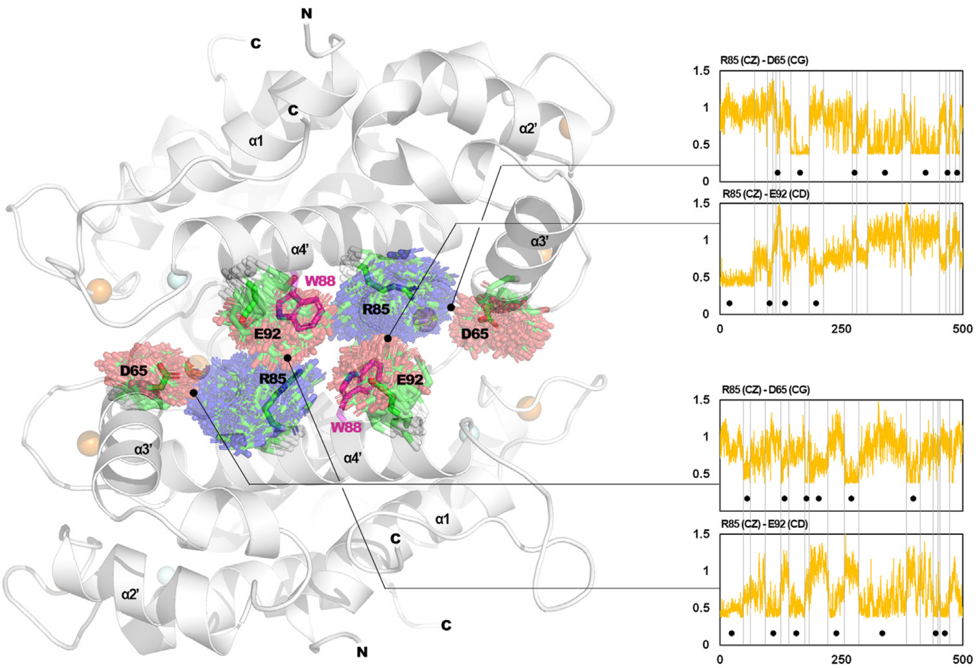

Figure 11. Interactions between helices IV_{A9} set up a dynamic gate protecting the dimer–dimer interface from solvent access. The evolution plots of respective distances are aligned to demonstrate the alternating interchangeable switching between interactions (schematically marked with *black dots* based on distance).

therefore could be used as an implicit but more feasible measure of this property for other, for example, posttranslationally modified, proteoforms.

The strong hydrophobic interactions between helices I in $(S100A8)_2$ may be the reason for a kinetic inhibition of the native homodimer's rearrangement to the thermodynamically more stable heterodimer both *in vivo* and *in vitro*; disassembly of homodimers at low pH and refolding to neutral pH leads to preferential heterodimer formation (20).

HDx kinetics, PLIMSTEX, and native MS have been used recently to study Ca^{2+} binding to the $C42S_{A8}C3S_{A9}$ mutant of calprotectin (39). Despite differences in the details of the procedures, our experiments on wildtype protein yielded results consistent with the C to S–mutant data. The set of identified peptic peptides was similar, and analogous regions in the wildtype and mutant complexes have similar HDx properties, suggesting that the mutations do not influence the Ca^{2+} binding properties of the heterodimer. Under the experimental conditions in this work, at the Ca^{2+}:calprotectin ratio of 5:1, the formation of tetramers is already advanced, and the dynamics of HDx rates show sharp changes for both canonical loops and a flatter profile for the S100A9 noncanonical loop. In S100A8, the noncanonical loop is insensitive to any Ca^{2+} excess, suggesting it is dispensable for tetramerization. This is consistent with the previously proposed scenario that tetramer formation might start right after the filling of both the canonical and S100A9 noncanonical loops with Ca^{2+}. Experiments with Zn^{2+} provided additional insight. Calprotectin already assembles into tetramers at the Zn^{2+}:protein ratio of 0.5:1, so only one ion is sufficient for this process.

Studies on transition metal ion binding to the calprotectin showed that the preferred binding site for Zn^{2+} is the H3D site involving the $D30_{A9}$ side chain. Thus, Zn^{2+} transitively reduces the dynamics of the S100A9 canonical loop.

The canonical loop in S100A8 ($A8_{59-68}$) is represented by a peptic peptide that displays two isotopic envelopes after the tetramer forms, and this impaired stability may have its source in the immediate structural neighborhood and its context within the tetramer. Specifically, helix III_{A9} preceding the canonical loop of S100A9 is buried between two heterodimers. It packs onto the S100A8 noncanonical loop and S100A9 C-terminal tail of the incoming dimer, while in S100A8 it is exposed and away from the dimer–dimer interface. Consequently, unlike helix III_{A8}, its counterpart from S100A9 does not display the dual appearance of isotopic envelopes and converges straight into its final conformation. Differences in the stability of helices III might directly affect the canonical loops, hence the imperfect stability in S100A8. The sustained presence of double isotopic envelopes during Zn^{2+}-induced tetramerization also suggests that the calprotectin tetramer maintains some flexibility within the loops; however, to reach an ultimately stable conformation, these must become geometrically rigid upon Ca^{2+} binding.

Calprotectin assembles into higher oligomers in the presence of Zn^{2+} ions, with and without Ca^{2+}. Although the process, in most cases, leads to tetramer formation, it may also result in the formation of higher oligomers. Because Zn^{2+} ions do not occupy the Ca^{2+} loops but localize to specific sites nearby, the mechanistic details are different. They predominantly include implicit stabilization of S100A9 loops upon securing the $D30_{A9}$-Zn^{2+} interaction. A similar effect has been described for the H3D site in the crystal structures of Mn^{2+}- and Ni^{2+}-calprotectin complexes (7, 28, 41, 42). The H6 Zn^{2+}-binding site seems to be less rigid. Interaction of Zn^{2+} ions with optional histidines or thiols from beyond the transient metal-binding sites might allow for the formation of other, noncanonical oligomers. In addition, since the interaction between Zn^{2+} ion and histidine depends on the protonation state of the latter, the Zn^{2+}-dependent oligomerization might be sensitive to pH changes.

The interactions between tetramers are an unexplored phenomenon. Interestingly, all X-ray structures contain more than one tetramer (7, 15, 28, 41, 42). Remarkably, all asymmetric units for structures solved with the H6 site occupied with a transition metal, be it Mn^{2+} (pdb|4ggf, pdb|4xjk) or Ni^{2+} (pdb|5w1f, pdb|6ds2), contain tetramers contacting each other through the S100A8 noncanonical loops (7, 28, 41, 42). In pdb|4xjk, the noncanonical loop of S100A8 interacts with the rim of the H6 site: the C-terminal tail of S100A9 of the other tetramer, which is also stabilized upon ion binding. The only tetrameric structure lacking transition metals shows no immediate interaction between tetramers within the asymmetrical unit. Calprotectin forms amyloid fibrils 4 to 8 nm in diameter in the presence of excess Zn^{2+} ions (30). A single chain of tetramers binding through their S100A8 noncanonical loops would have a diameter of about 44 Å, which is compatible with observed microscopic properties. However, additional studies might be needed to verify the nature of such tetramer–tetramer interactions.

Conclusions

We have identified conformational changes between multiple proteoforms of S100A8 and S100A9 proteins. The methods used allowed us to study even minute changes to calprotectin's dynamical properties that have not been reported previously. We show that the conserved S100 proteins' 3D-structural plasticity should be regarded as an essential aspect of S100A8 and S100A9 regulation. The changing flexibility and accessibility of specific regions in different proteoforms may allow binding surfaces to adapt to their diverse target proteins. Such conclusions agree with the increasing number of observations that, despite the general sequence-to-structure relationship, the proteins' plasticity shapes how they interact within their biological context (43).

As the technique has few molecular weight and buffer limitations, we propose HDx-MS as a method of choice for differential studies of the multitude of S100A8 and S100A9 interactors that have been described biochemically but not structurally. It can be successfully applied to unmodified proteins, making it a solid basis for future research on the regulatory effects of posttranslational modifications, including redox modifications of cysteine thiols. Understanding the relationships between conformational dynamics and biological properties such as proteolytic susceptibility, oligomerization potential, and the formation of target-specific binding sites given by the combination of HDx-MS and MD should provide rationales for developing screening tests or targeted medicines.

Recognizing specific interactions that maintain proteoforms without bound metal ions is a starting point for the design of mutants that could allow the intracellular functions of homo- and heterodimers to be distinguished, as has been done successfully with mutants in calcium loops for the heterodimer and tetramer (3, 44, 45). Such methods would be indispensable in explaining the many contradictory studies regarding the effects of intracellular S100A8 and S100A9, by distinguishing between proteoforms that may exhibit different activities.

Experimental procedures

Overexpression and purification of the recombinant S100A8 and S100A9 proteins

Recombinant wildtype human S100A8 and S100A9 proteins without purification tags were overexpressed in *E. coli* as described in detail in the supporting information. They were purified from solubilized bacterial inclusion bodies using reverse-phase (RP) HPLC. Pure protein fractions were collected, lyophilized, and stored at −80 °C. The identity and purity of proteins were confirmed using analytical RP HPLC and electrospray mass spectrometry of whole proteins. The concentration of the proteins in solutions was quantified by UV absorbance at 280 nm. The absorption coefficients were taken from the literature (1.03 ml/mg^{-1} cm^{-1} for S100A8, 0.526 ml/mg^{-1} cm^{-1} for S100A9, and 0.75 ml/mg^{-1} cm^{-1} for calprotectin, for dimers) (20).

Refolding of denatured S100A8 and S100A9 proteins

Lyophilized denatured proteins were dissolved in 0.1 M glycine buffer, pH 2.5 to a final concentration of 100 μM. Homodimers were prepared by renaturation of individual S100A8 or S100A9 proteins in glycine buffers by stepwise dialysis to 20 mM TES, 50 mM NaCl, pH 8.0 (for $(S100A8)_2$) or 20 mM TES, 100 mM NaCl, pH 7.5 (for $(S100A9)_2$) using Spectra/Por 3 3.5 kD MWCO (Spectrum Labs) dialysis tubes. To obtain the S100A8/S100A9 heterodimer, a mixture of the same volumes of equimolar glycine buffer solutions of both proteins was dialyzed to 20 mM TES pH 7.5, 100 mM NaCl.

All buffers were treated with Chelex 100 Resin before use to remove traces of metal ions. If necessary, a 10-fold molar excess of tris-(2-carboxyethyl)phosphine (TCEP) was added to reduce any disulfide bonds.

Purification of refolded complexes

The refolded protein solutions were adjusted to a concentration of 80 to 100 μM, centrifuged at 4 °C for 1 min at 14,000 rpm to get rid of any unspecific higher aggregates, and purified using anion exchange chromatography on a HiTrap Q HP column (GE Lifesciences) connected to an ÄKTA purifier (GE Lifesciences) at 10 °C with a 0.5 μl/min flow rate. In detail, 2000 μl of the protein sample was loaded into a column equilibrated with solvent A (20 mM TES pH 7.5, 20 mM NaCl) and eluted with an increasing gradient (0%–60% in 35 min) of solvent B (20 mM TES pH 7.5, 1 M NaCl) with protein detection at 280 nm. The subunit content, purity, and the reduced state of cysteine thiols were confirmed using analytical

RP HPLC, LC-ESI-MS, and SDS-PAGE (Fig. S1). Fractions containing purified expected proteins were collected, the buffer was exchanged to 20 mM TES pH 7.5, 100 mM NaCl and samples at a final protein concentration of 80 to 100 μM were passed through a size-exclusion column to select a single oligomeric species for further analyses.

Analytical size-exclusion chromatography

A volume of 100 μl of a 50 μM protein complex solution in 20 mM TES pH 7.5, 100 mM NaCl was loaded onto an equilibrated Superdex 75 5/150 GL column (GE Healthcare) connected to the ÄKTA purifier (GE Lifesciences) at a flow rate of 0.5 ml/min at 20 °C.

To determine the oligomerization status of complexes in the presence of divalent metal ions before SEC analysis, samples were incubated with a metal ion for 15 min at 4 °C and centrifuged for 1 min at 14,000 rpm. The final concentration of Ca^{2+} ($CaCl_2$ salt) was 1 mM and the final concentrations of Zn^{2+} ($ZnCl_2$ salt) were 50, 75, and 100 μM. For the analysis with Ca^{2+}-induced oligomerization, the SEC running buffer included 1 mM $CaCl_2$. The protein elution peaks were detected by UV absorbance at 280 nm, collected, and analyzed by LC-ESI-MS and SDS-PAGE under reducing and nonreducing conditions. The oligomer sizes were estimated using a Bio-Rad gel filtration standard containing mass markers ranging from 1.35 kDa to 670 kDa (vitamin B12, 1.35 kDa; myoglobin, 17 kDa; ovalbumin, 44 kDa; γ-globulin, 158 kDa; and thyroglobulin, 670 kDa).

Analytical ultracentrifugation

Sedimentation velocity measurements were carried out in a Beckman-Coulter ProteomeLab XL-I analytical ultracentrifuge equipped with an An-50 8-hole analytical rotor, 12-mm path length, and double-sector charcoal-Epon cells. The protein samples prior to analysis were incubated for 15 min at 4 °C with metal ions and measured at a concentration of 0.5 mg/ml in 20 mM TES pH 7.5, 100 mM NaCl in the absence and presence of a 20 molar excess per dimer of Ca^{2+} ($CaCl_2$ salt) and 1, 2, and 4 molar equivalents per dimer of Zn^{2+} ($ZnCl_2$ salt). The analytic cells containing 400 μl of sample and 410 μl of buffer in separate sectors were centrifuged at 50,000 rpm and monitored by UV absorbance at 280 nm at 20 °C, using a continuous scan mode and radial spacing of 0.003 cm. Data were analyzed using the "Continuous c(s) distribution" model of the SEDFIT program (46), with a confidence level (F-ratio) specified as 0.68. Solvent density (1.0047 g/cm^3) and viscosity (1.020 mPa s) were measured at 20 °C using an Anton Paar DMA 5000 densitometer and Lovis 2000 M rolling-ball viscometer, respectively. Partial specific volume and extinction coefficients for proteins were calculated using SEDNTERP software (47). The results were plotted using the GUSSI graphical program (48).

Circular dichroism spectroscopy

Far-UV CD

Protein samples after SEC purification were dialyzed to 20 mM TES pH 7.5 to remove NaCl and adjusted to the final protein concentration of 5.5 μM in a volume of 300 μl. To detect metal ion–induced changes, proteins were incubated with a 10-fold molar excess of Ca^{2+}, 2-fold excess of Zn^{2+}, or a combination of both ions, for 15 min at 4 °C. CD spectra were recorded from 270 nm to 195 nm.

Near-UV CD

Solutions of protein complexes after FPLC purification were adjusted to the final protein concentration of 1 mg/ml in a volume of 1500 μl. To detect metal ion–induced changes, calprotectin was incubated with a 2.5-, 5-, and 7.5-fold molar excess of Ca^{2+}, 0.1-, 0.25-, 0.5-, 0.75-, 1-, and 2-fold excess of Zn^{2+} for 15 min at 4 °C. Near-UV spectra were recorded from 360 nm to 240 nm.

All spectra (far-UV and near-UV CD) were recorded in a 1-mm path-length quartz CD cuvette (Hellma Analytics) with a J-815 CD Spectrometer (Jasco) at 20 °C. The blank buffer was used as a control. Wavelength scans were carried out with 1-nm intervals (2 s averaging time, three averaged scans). Molar ellipticity [θ] and mean residual ellipticity [θ]MRW were calculated according to the following formulas:

$$[\theta] = \theta / (c \cdot l)$$

$$[\theta]\mathrm{MRW} = \theta / (c \cdot l \cdot n)$$

where: θ is the measured ellipticity (millidegrees); c is the molar protein concentration; l is the optical path length of the cuvette (millimeters); n is the number of peptide bonds in a peptide, considering these numbers to be 185, 225, and 205, respectively, for $(S100A8)_2$, $(S100A9)_2$, and the calprotectin complex.

Native mass spectrometry

For native MS analyses, proteins were transferred using P-6 Micro BioSpin columns (Bio-Rad), from the nonvolatile TES buffer to a volatile 100 mM ammonium acetate (AmAc) buffer, pH 7.5. Native MS spectra were measured for 25 μM calprotectin in the presence of ammonium salts of 0, 1, 2, 4, 6, and 8 molar equivalents of the Ca^{2+} ion, or 0, 1, 2, 3, and 4 molar equivalents of Zn^{2+}. Using precut TaperTip emitters (Waters), the protein samples were introduced to a Q-TOF (Synapt G2 HDMS, Waters) mass spectrometer tuned to maintain the native structure of protein complexes. The MS settings (for samples without metal ions) with optimal ion transmission were as follows: 1.6 kV capillary voltage, 14 V sampling cone, 5 V extractor cone, 30 °C source temperature, 10 V trap collision energy, and 5 V transfer collision energy. MS settings for samples with metal ions were as follows: 1.8 kV capillary voltage, 100 V sampling cone, 5 V extractor cone, 30 °C source temperature, 50 V trap collision energy, and 5 V transfer collision energy. Pressures throughout the instrument were ~6 mbar backing, 3.1 mbar in the ion mobility cell, and 2.5*10−2 mbar for the trap and transfer cell, respectively. Deconvolution of the native mass spectra was performed using the online tool ESIprot (49).

Nano differential scanning fluorimetry

The thermal stability of $(S100A8)_2$, $(S100A9)_2$, and calprotectin in the absence of metal ions and after a 15-min incubation with 20 molar excess of Ca^{2+} at 4 °C was analyzed using a Prometheus NT.48 instrument (NanoTemper Technologies). Protein solutions (10 µl) with a final concentration of 25 µM in 20 mM TES, pH 7.5, 100 mM NaCl were loaded into capillaries (NanoTemper Technologies) and the fluorescence was monitored at 330 and 350 nm in duplicate. The thermal ramp was from 20 to 90 °C with a temperature slope of 1 °C/min. The denaturation data are presented as the 350 nm:330 nm fluorescence ratio *versus* temperature. The melting temperatures for each complex were calculated using the producer-provided PR.ThermControl software.

Hydrogen–deuterium exchange reactions

The solutions of purified refolded protein complexes were buffer-exchanged to 20 mM TES pH 7.5, 100 mM NaCl. Protein concentrations were adjusted to 50 µM. For experiments with metal ions, solutions of appropriate apo dimers were incubated with either a 20-fold molar excess of Ca^{2+} ($CaCl_2$ salt), a 1- and 2-fold molar equivalent, per dimer, of Zn^{2+} ($ZnCl_2$ salt), or a combination of both ions for 15 min at 4 °C.

To initiate the hydrogen–deuterium exchange, 5 µl of appropriate oligomer solution was diluted with a 9-fold excess (45 µl) of a D_2O buffer (20 mM TES buffer pH 7.5, 100 mM NaCl in 99.9% D_2O) at 25 °C. Aliquots of the solutions were taken at various time points after the addition of D_2O: immediately, at 10 s; and at 1 min, 5 min, or 24 h, added to 10 µl of an ice-cold quench buffer (2 M glycine pH 2.5 in D_2O) to stop the hydrogen/deuterium exchange reaction, and immediately frozen at −80 °C. For further calculations, samples analyzed immediately after D_2O addition were considered minimally labeled, and after 24 h of exchange, maximally labeled. All HDx experiments were repeated in triplicate.

Detection of deuterium uptake in proteins based on mass spectrometry of peptic peptides

First, for all studied proteoforms, stock solutions of homogeneous complexes were diluted to the final concentration of 5 µM in 20 mM TES, pH 7.5, 100 mM NaCl, in H_2O. A volume of 50 µl of the 5 µM solutions were mixed with 10 µl of ice-cold 2 M glycine buffer pH 2.5 in H_2O and immediately passed through an immobilized pepsin column (Poroszyme Immobilized Pepsin). The peptic peptides were (i) desalted by passing through a directly connected C18 precolumn (2.1 × 5 mm, ACQUITY BEH C18 VanGuard precolumn, 1.7 µM resin, Waters) using 0.07% formic acid (FA) in water run at 200 µl/min; (ii) separated on a C18 reversed-phase column (1.0 × 50 mm, ACQUITY UPLC-BEH reversed-phase column, 1.7 µM resin, Waters) with a gradient of solvent A (0.1% FA in water) and solvent B (0.1% FA in 90% acetonitrile in water) with a 90-µl/min flow rate; and (iii) analyzed using a SYNAPT G2 HDMS (Waters) mass spectrometer. ProteinLynx Global SERVER software (PLGS, Waters) was used to identify the sequences of detected peptides with the criteria of acceptance as 0.3 minimum products per amino acid and a minimum intensity threshold of 3000. A common set of peptides detected in each proteoform was determined and covered 93% of S100A8 and S100A9 sequences. The common peptides were used to measure and compare the deuterium uptakes between proteins under different experimental conditions.

Samples frozen after HDx reactions were individually thawed and processed in exactly the same manner as described above for samples in H_2O for peptic peptide identifications. However, D_2O replaced H_2O in all elution buffers and the mass spectrometer worked in the LC-MS mode, without peptide sequencing. All LC-MS analyses were carried out at 0.5 °C.

Analysis of HDx-MS data

DynamX 3.0 software (Waters) was used to determine the deuterium uptake for peptic peptides common to all proteoforms based on the HDx-MS experimental results. The peak assignments to isotopic envelopes were manually curated in all mass spectra. If fragmentary envelopes were proposed by the software, full envelopes were searched for in the spectra. Experimental peptide retention times and molecular weights were exported, and the percentage of peptide deuteration (D%) was calculated using Excel according to the formula:

$$D(\%) = \frac{(M_{ex} - M_{ex}0)}{(M_{ex}100 - M_{ex}0)} * 100\%$$

where M_{ex} is the molecular weight of a peptide at specific incubation time, $M_{ex}0$ is the molecular weight of a peptide with a minimum exchange, and $M_{ex}100$ is the molecular weight of a peptide with maximum exchange.

Error bars for deuterium uptake in three replicates of measurements were calculated as standard deviations. The deuterium uptakes were calculated using Excel software (Microsoft Office), and graphs were plotted with OriginPro (OriginLab) software.

Bimodal isotopic distribution analysis

Some peptic peptides could be assigned in the metal-ion titration experiments to two separate isotopic envelopes (Fig. 6, *A* and *C*), indicating the presence of two different conformations for the metal ion—loaded and unloaded proteoforms in their protein region. For such peptides, we calculated the contributions of the two observed conformers. For this, a set of 200 theoretical uniformly deuterated single-state distributions ranging from 0% to 100% deuterium uptake was simulated for selected peptides. For the deconvolution procedure, both centroided experimental distributions and theoretical distributions were represented as 500-element vectors, calculated by convolution with a Gaussian function and sampling at points uniformly distributed along the specified mass range. The resulting linear equations were solved using a boosted Gold algorithm as described in Mohrac *et al.*, with 10,000 iterations, 100 boosting steps, and $p = 1.2$. This allowed us to obtain a linear combination of single-state distributions that fits the measured distribution while meeting physical constraints (a small number of nonzero elements, no negative elements). In case of two neighboring nonzero elements in the solution vector, only a single component distribution is reported in the results, with deuterium uptake linearly interpolated between theoretical uptakes corresponding to these elements (50).

Protein–ligand interaction in solution by mass spectrometry, titration, and hydrogen/deuterium exchange experiment

For PLIMSTEX titration experiments, individual 5-μl aliquots of 40 μM calprotectin were incubated for 15 min at 4 °C with increasing amounts of Ca^{2+} ($CaCl_2$ salt) or Zn^{2+} ($ZnCl_2$ salt) ions. The following molar equivalents were used for Ca^{2+}: 0, 0.05, 1.25, 1.75, 2.5, 5, 7, 5, 10, 20, 25, 40, and 50, and for Zn^{2+}: 0, 0.1, 0.25, 0.5, 1, 1.25, 1.75, 2, 2.25, 2.5, 3, and 4. After incubation with metal ions, the samples were diluted with D_2O and the HDx reaction was run for 5 min at 25 °C. Further HDx-MS procedures and data analyses were conducted as described above. PLIMSTEX runs were repeated at least twice for every metal ion:protein ratio.

Molecular dynamics simulations and structure visualization

MD simulations in an environment corresponding to physiological solution have been performed to assess the conformational stability of all oligomers studied in this project. Initial structures were obtained from the PDB database: pdb|5i8n for S100A9 homodimer, pdb|5hlo for S100A8 homodimer, pdb|4ggf for S100A8/S100A9 heterodimer and heterotetramer. All nonprotein molecules were removed from the PDB structures, except for the Ca^{2+} ions for respective runs. Residue mutations or sequence deletions present in the PDB structures were reversed prior to simulations. All MD simulations were carried out using GROMACS 2020.3 software (51) with a CHARMM36 (July 2020) force field (52) and the TIP3P water model.

All structure 3D representations were rendered in Pymol (www.pymol.org).

Data availability

Raw data and derived data supporting the findings of this study are available from the corresponding author (A. W.-C.) on request.

Supporting information—This article contains supporting information (7, 15, 28, 29, 41, 42, 53–56).

Acknowledgments—We thank Jacek Olędzki for LC-MS technical help, Lilia Zhukova for help with protein expression and purification, Alexander Moysa for an introduction to native-MS experiments, and Michał Kistowski for bimodal isotopic distribution analysis. This work was supported by the Polish National Science Center (2016/21/B/NZ1/02788), and in part by PLGrid Infrastructure (79/E-35/SPUB/SP/2019 grant) and POL-OPENSCREEN (DIR/Wk/2018/06).

Author contributions—A. W.-C. conceptualization; M. P. and K. S. methodology; K. S. formal analysis; M. P. and R. H. S. investigation; M. P., K. S., and R. H. S. data curation; A. W.-C., M. P., and K. S. writing – original draft; A. W.-C. writing – review & editing; M. P. and K. S. visualization; A. W.-C. supervision.

Conflict of interest—The authors declare that they have no conflicts of interest with the contents of this article.

Abbreviations—The abbreviations used are: CD, circular dichroism; ESI, electrospray ionization; FA, formic acid; HDx, hydrogen-deuterium exchange; LC, liquid chromatography; MD, molecular dynamics; MS, mass spectrometry; PLIMSTEX, protein-ligand interaction in solution by mass spectrometry, titration, and HDx; RP, reverse phase; SEC, size-exclusion chromatography; TES, N-[tris(hydroxymethyl)methyl]-2-aminoethanesulfonic acid, 2-[(2-hydroxy-1, 1-bis(hydroxymethyl)ethyl)amino]ethanesulfonic acid.

References

1. Jukic, A., Bakiri, L., Wagner, E. F., Tilg, H., and Adolph, T. E. (2021) Calprotectin: from biomarker to biological function. *Gut* **70**, 1978–1988
2. Donato, R., Cannon, B. R., Sorci, G., Riuzzi, F., Hsu, K., Weber, D. J., *et al.* (2013) Functions of S100 proteins. *Curr. Mol. Med.* **13**, 24–57
3. Vogl, T., Stratis, A., Wixler, V., Völler, T., Thurainayagam, S., Jorch, S. K., *et al.* (2018) Autoinhibitory regulation of S100A8/S100A9 alarmin activity locally restricts sterile inflammation. *J. Clin. Invest.* **128**, 1852–1866
4. Wang, S., Song, R., Wang, Z., Jing, Z., Wang, S., and Ma, J. (2018) S100A8/A9 in inflammation. *Front. Immunol.* **9**, 1298
5. Leclerc, E., Fritz, G., Vetter, S. W., and Heizmann, C. W. (2009) Binding of S100 proteins to RAGE: an update. *Biochim. Biophys. Acta* **1793**, 993–1007
6. Zygiel, E. M., and Nolan, E. M. (2018) Transition metal sequestration by the host-defense protein calprotectin. *Annu. Rev. Biochem.* **87**, 621–643
7. Damo, S. M., Kehl-Fie, T. E., Sugitani, N., Holt, M. E., Rathi, S., Murphy, W. J., *et al.* (2013) Molecular basis for manganese sequestration by calprotectin and roles in the innate immune response to invading bacterial pathogens. *Proc. Natl. Acad. Sci. U. S. A.* **110**, 3841–3846
8. Xu, Z., Cheng, C., Kong, R., Liu, Y., Wang, S., Ma, Y., *et al.* (2021) S100A8 and S100A9, both transcriptionally regulated by PU.1, promote epithelial-mesenchymal transformation (EMT) and invasive growth of dermal keratinocytes during scar formation post burn. *Aging (Albany NY)* **13**, 15523–15537
9. Gheibi, N., Ghorbani, M., Shariatifar, H., and Farasat, A. (2020) Effects of unsaturated fatty acids (arachidonic/oleic acids) on stability and structural properties of calprotectin using molecular docking and molecular dynamics simulation approach. *PLoS One* **15**, e0230780
10. Jia, J., Arif, A., Terenzi, F., Willard, B., Plow, E. F., Hazen, S. L., *et al.* (2014) Target-selective protein S-nitrosylation by sequence motif recognition. *Cell* **159**, 623–634
11. Rosenberger, S., Thorey, I. S., Werner, S., and Boukamp, P. (2007) A novel regulator of telomerase: s100A8 mediates differentiation-dependent and calcium-induced inhibition of telomerase activity in the human epidermal keratinocyte line HaCaT*. *J. Biol. Chem.* **282**, 6126–6135
12. Stark, C., Breitkreutz, B.-J., Reguly, T., Boucher, L., Breitkreutz, A., and Tyers, M. (2006) BioGRID: a general repository for interaction datasets. *Nucleic Acids Res.* **34**, D535–D539

13. Chatziparasidis, G., and Kantar, A. (2021) Calprotectin: an ignored biomarker of neutrophilia in pediatric respiratory diseases. *Children (Basel)* **8**, 428
14. Allgöwer, C., Kretz, A.-L., von Karstedt, S., Wittau, M., Henne-Bruns, D., and Lemke, J. (2020) Friend or foe: S100 proteins in cancer. *Cancers (Basel)* **12**, 2037
15. Korndörfer, I. P., Brueckner, F., and Skerra, A. (2007) The crystal structure of the human (S100A8/S100A9)2 heterotetramer, calprotectin, illustrates how conformational changes of interacting α-helices can determine specific association of two EF-hand proteins. *J. Mol. Biol.* **370**, 887–898
16. Permyakov, S. E., Ismailov, R. G., Xue, B., Denesyuk, A. I., Uversky, V. N., and Permyakov, E. A. (2011) Intrinsic disorder in S100 proteins. *Mol. Biosyst.* **7**, 2164–2180
17. Edgeworth, J., Gorman, M., Bennett, R., Freemont, P., and Hogg, N. (1991) Identification of p8,14 as a highly abundant heterodimeric calcium binding protein complex of myeloid cells. *J. Biol. Chem.* **266**, 7706–7713
18. Vogl, T., Gharibyan, A. L., and Morozova-Roche, L. A. (2012) Pro-inflammatory S100A8 and S100A9 proteins: self-assembly into multifunctional native and amyloid complexes. *Int. J. Mol. Sci.* **13**, 2893–2917
19. Källberg, E., Tahvili, S., Ivars, F., and Leanderson, T. (2018) Induction of S100A9 homodimer formation *in vivo*. *Biochem. Biophys. Res. Commun.* **500**, 564–568
20. Vogl, T., Leukert, N., Barczyk, K., Strupat, K., and Roth, J. (2006) Biophysical characterization of S100A8 and S100A9 in the absence and presence of bivalent cations. *Biochim. Biophys. Acta* **1763**, 1298–1306
21. Uhlén, M., Fagerberg, L., Hallström, B. M., Lindskog, C., Oksvold, P., Mardinoglu, A., *et al.* (2015) Tissue-based map of the human proteome. *Science* **347**, 1260419
22. Tardif, M. R., Chapeton-Montes, J. A., Posvandzic, A., Pagé, N., Gilbert, C., and Tessier, P. A. (2015) Secretion of S100A8, S100A9, and S100A12 by neutrophils involves reactive oxygen species and potassium efflux. *J. Immunol. Res.* **2015**, 296149
23. Fritz, G., and Heizmann, C. (2006) *3D Structures of the Calcium and Zinc Binding S100 Proteins*, John Wiley & Sons, Ltd, Hoboken, NJ
24. Gilston, B. A., Skaar, E. P., and Chazin, W. J. (2016) Binding of transition metals to S100 proteins. *Sci. China Life Sci.* **59**, 792–801
25. Lim, S. Y., Raftery, M., Cai, H., Hsu, K., Yan, W. X., Hseih, H.-L., *et al.* (2008) S-nitrosylated S100A8: novel anti-inflammatory properties. *J. Immunol.* **181**, 5627–5636
26. Lim, S. Y., Raftery, M. J., Goyette, J., and Geczy, C. L. (2010) S-glutathionylation regulates inflammatory activities of S100A9. *J. Biol. Chem.* **285**, 14377–14388
27. Hoskin, T. S., Crowther, J. M., Cheung, J., Epton, M. J., Sly, P. D., Elder, P. A., *et al.* (2019) Oxidative cross-linking of calprotectin occurs *in vivo*, altering its structure and susceptibility to proteolysis. *Redox Biol.* **24**, 101202
28. Nakashige, T. G., Zygiel, E. M., Drennan, C. L., and Nolan, E. M. (2017) Nickel sequestration by the host-defense protein human calprotectin. *J. Am. Chem. Soc.* **139**, 8828–8836
29. Lin, H., Andersen, G. R., and Yatime, L. (2016) Crystal structure of human S100A8 in complex with zinc and calcium. *BMC Struct. Biol.* **16**, 8
30. Yanamandra, K., Alexeyev, O., Zamotin, V., Srivastava, V., Shchukarev, A., Brorsson, A.-C., *et al.* (2009) Amyloid formation by the pro-inflammatory S100A8/A9 proteins in the ageing prostate. *PLoS One* **4**, e5562
31. Stephan, J. R., Yu, F., Costello, R. M., Bleier, B. S., and Nolan, E. M. (2018) Oxidative post-translational modifications accelerate proteolytic degradation of calprotectin. *J. Am. Chem. Soc.* **140**, 17444–17455
32. Xiao, Y., Shaw, G. S., and Konermann, L. (2017) Calcium-mediated control of S100 proteins: allosteric communication via an agitator/signal blocking mechanism. *J. Am. Chem. Soc.* **139**, 11460–11470
33. Bajor, M., Zaręba-Kozioł, M., Zhukova, L., Goryca, K., Poznański, J., and Wysłouch-Cieszyńska, A. (2016) An interplay of S-nitrosylation and metal ion binding for astrocytic S100B protein. *PLoS One* **11**, e0154822
34. Narang, D., Lento, C., and J Wilson, D. (2020) HDX-MS: an analytical tool to capture protein motion in action. *Biomedicines* **8**, 224
35. Giladi, M., and Khananshvili, D. (2020) Hydrogen-deuterium exchange mass-spectrometry of secondary active transporters: from structural dynamics to molecular mechanisms. *Front. Pharmacol.* **11**, 70
36. Masson, G. R., Burke, J. E., Ahn, N. G., Anand, G. S., Borchers, C., Brier, S., *et al.* (2019) Recommendations for performing, interpreting and reporting hydrogen deuterium exchange mass spectrometry (HDX-MS) experiments. *Nat. Methods* **16**, 595–602
37. NematiNiko, F., Chegini, K. G., Asghari, H., Amini, A., and Gheibi, N. (2017) Modifying effects of carboxyl group on the interaction of recombinant S100A8/A9 complex with tyrosinase. *Biochim. Biophys. Acta* **1865**, 370–379
38. Imani, M., Bahrami, Y., Jaliani, H. Z., and Ardestani, S. K. (2014) In solution cation-induced secondary and tertiary structure alterations of human calprotectin. *Protein J.* **33**, 465–473
39. Adhikari, J., Stephan, J. R., Rempel, D. L., Nolan, E. M., and Gross, M. L. (2020) Calcium binding to the innate immune protein human calprotectin revealed by integrated mass spectrometry. *J. Am. Chem. Soc.* **142**, 13372–13383
40. Nacken, W., and Kerkhoff, C. (2007) The hetero-oligomeric complex of the S100A8/S100A9 protein is extremely protease resistant. *FEBS Lett.* **581**, 5127–5130
41. Gagnon, D. M., Brophy, M. B., Bowman, S. E. J., Stich, T. A., Drennan, C. L., Britt, R. D., *et al.* (2015) Manganese binding properties of human calprotectin under conditions of high and low calcium: X-ray crystallographic and advanced electron paramagnetic resonance spectroscopic analysis. *J. Am. Chem. Soc.* **137**, 3004–3016
42. Nakashige, T. G., Bowman, S. E. J., Zygiel, E. M., Drennan, C. L., and Nolan, E. M. (2018) Biophysical examination of the calcium-modulated nickel-binding properties of human calprotectin reveals conformational change in the EF-hand domains and His3Asp site. *Biochemistry* **57**, 4155–4164
43. Montioli, R., Sgaravizzi, G., Desbats, M. A., Grottelli, S., Voltattorni, C. B., Salviati, L., *et al.* (2021) Molecular and cellular studies reveal folding defects of human ornithine aminotransferase variants associated with gyrate atrophy of the choroid and retina. *Front. Mol. Biosci.* **8**, 695205
44. Leukert, N., Vogl, T., Strupat, K., Reichelt, R., Sorg, C., and Roth, J. (2006) Calcium-dependent tetramer formation of S100A8 and S100A9 is essential for biological activity. *J. Mol. Biol.* **359**, 961–972
45. Stephan, J. R., and Nolan, E. M. (2016) Calcium-induced tetramerization and zinc chelation shield human calprotectin from degradation by host and bacterial extracellular proteases. *Chem. Sci.* **7**, 1962–1975
46. Schuck, P. (2000) Size-distribution analysis of macromolecules by sedimentation velocity ultracentrifugation and Lamm equation modeling. *Biophys. J.* **78**, 1606–1619
47. Philo, J. S. (2011) Limiting the sedimentation coefficient for sedimentation velocity data analysis: partial boundary modeling and g(s*) approaches revisited. *Anal. Biochem.* **412**, 189–202
48. Brautigam, C. A. (2015) Chapter five - calculations and publication-quality illustrations for analytical ultracentrifugation data. In: Cole, J. L., ed., *Methods in Enzymology* **562**. Academic Press, Cambridge, Massachusetts: 109–133
49. Winkler, R. (2010) ESIprot: a universal tool for charge state determination and molecular weight calculation of proteins from electrospray ionization mass spectrometry data. *Rapid Commun. Mass Spectrom.* **24**, 285–294
50. Przygońska, K., Poznański, J., Mistarz, U. H., Rand, K. D., and Dadlez, M. (2018) Side-chain moieties from the N-terminal region of Aβ are Involved in an oligomer-stabilizing network of interactions. *PLoS One* **13**, e0201761
51. Abraham, M. J., Murtola, T., Schulz, R., Páll, S., Smith, J. C., Hess, B., *et al.* (2015) GROMACS: high performance molecular simulations through multi-level parallelism from laptops to supercomputers. *SoftwareX* **1–2**, 19–25
52. Huang, J., and MacKerell, A. D., Jr. (2013) CHARMM36 all-atom additive protein force field: validation based on comparison to NMR data. *J. Comput. Chem.* **34**, 2135–2145

53. Ishikawa, K., Nakagawa, A., Tanaka, I., Suzuki, M., and Nishihira, J. (2000) The structure of human MRP8, a member of the S100 calcium-binding protein family, by MAD phasing at 1.9 Å resolution. *Acta Crystallogr. D Biol. Crystallogr.* **56**, 559–566
54. Chang, C.-C., Khan, I., Tsai, K.-L., Li, H., Yang, L.-W., Chou, R.-H., *et al*. (2016) Blocking the interaction between S100A9 and RAGE V domain using CHAPS molecule: a novel route to drug development against cell proliferation. *Biochim. Biophys. Acta* **1864**, 1558–1569
55. Itou, H., Yao, M., Fujita, I., Watanabe, N., Suzuki, M., Nishihira, J., *et al.* (2002) The crystal structure of human MRP14 (S100A9), a Ca2+-dependent regulator protein in inflammatory process. *J. Mol. Biol.* **316**, 265–276
56. Brophy, M. B., Hayden, J. A., and Nolan, E. M. (2012) Calcium ion gradients modulate the zinc affinity and antibacterial activity of human calprotectin. *J. Am. Chem. Soc.* **134**, 18089–18100